One Earth

Article

Residential segregation and outdoor urban moist heat stress disparities in the United States

Graphical abstract

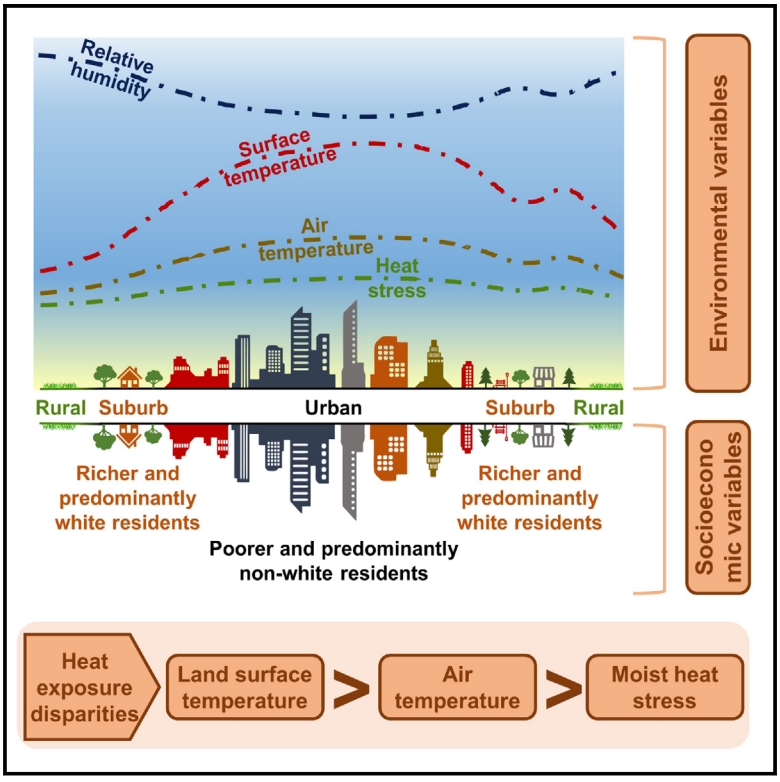

Highlights

- Urban-resolving numerical model shows pervasive heat stress disparities in US cities
- Present residential segregation strongly associated with heat stress inequities
- Historically redlined neighborhoods show higher heat stress than other neighborhoods
- Skin temperature overestimates disparities in ambient heat exposure and heat stress

Authors

TC Chakraborty, Andrew J. Newman, Yun Qian, Angel Hsu, Glenn Sheriff

Correspondence

tc.chakraborty@pnnl.gov

In brief

Although satellite-derived land-surface temperature is often used as a proxy for urban heat exposure disparities, this variable is not equivalent to heat stress. Here, we show pervasive income- and race-based inequities in summertime air temperature and moist heat stress in US cities. The magnitudes of these disparities are, however, smaller than those for land-surface temperature. These results are important for accurately capturing heat-related environmental distributional inequities for both monitoring risk to vulnerable populations and informing urban climate adaptation strategies.

Chakraborty et al., 2023, One Earth 6, 738–750
June 16, 2023
https://doi.org/10.1016/j.oneear.2023.05.016

CellPress

CellPress
OPEN ACCESS

One Earth

Article

Residential segregation and outdoor urban moist heat stress disparities in the United States

TC Chakraborty,[1,5,*] Andrew J. Newman,[2] Yun Qian,[1] Angel Hsu,[3] and Glenn Sheriff[4]
[1]Atmospheric Sciences and Global Change Division, Pacific Northwest National Laboratory, Richland, WA 99354, USA
[2]Research Applications Laboratory, National Center for Atmospheric Research, Boulder, CO 80307, USA
[3]School of Public Policy, University of North Carolina-Chapel Hill, Abernethy Hall, Chapel Hill, NC 27599, USA
[4]School of Politics and Global Studies, Arizona State University, PO Box 873902, Tempe, AZ 85297, USA
[5]Lead contact
*Correspondence: tc.chakraborty@pnnl.gov
https://doi.org/10.1016/j.oneear.2023.05.016

SCIENCE FOR SOCIETY Disparities in urban heat exposure have been widely studied using satellite-derived land-surface temperature. Due to observational and modeling limitations, it is unknown how the disparities seen for land-surface temperature relate to physiologically relevant heat exposure metrics, which have direct public health implications. Here, we show pervasive income- and race-based inequities in summertime air temperature and heat stress in US cities, providing national-scale evidence of heat-related urban environmental disparities. However, the magnitudes of air temperature and heat stress disparities are weaker than those for land-surface temperature. Thus, policy makers should be careful about relying on direct estimates from satellites to quantify urban heat exposure, due to their tendency to overestimate heat stress disparities. More observations and improved urban-scale models can fill this gap and provide actionable data for planning optimum and equitable urban heat mitigation strategies.

SUMMARY

The combined impact of urbanization-induced warming and drying on large-scale heat stress disparities remains unknown, with multicity studies using satellite-derived land surface temperature as a proxy for these disparities. Here, using high-resolution urban-resolving numerical model simulations for 2014–2018, we find pervasive disparities in all-sky average maximum summertime air temperature and moist heat stress metrics across US cities, with higher outdoor heat stress exposure in poorer and primarily non-white census tracts. Ninety-four percent of the US urban population (228 million) live in cities where heat stress burdens the poor, with heat stress inequities between white and non-white populations strongly associated with residential segregation. Similarly, historically redlined neighborhoods show higher heat stress than their non-redlined counterparts, demonstrating how historical segregation relates to present-day environmental inequalities. Our results provide quantitative estimates of physiologically relevant heat stress disparities at the US national scale and highlight potential biases when using satellites as a proxy for these.

INTRODUCTION

Urbanization is the most concentrated modification of the environment and human society through both physical changes and dynamic social and cultural paradigm shifts.[1–3] Currently, over half of the world's population resides in cities, which is expected to increase to around 66% by 2050.[4] While global rural-to-urban population migration gives cities easy access to human capital,[5] the durable nature of urban infrastructure can magnify inequalities between population groups and lock them in.[6] For instance, urban areas can have large variability in land cover and use, frequently reinforced by both historical and prevailing policies,[7] which can result in pervasive disparities in both basic access to amenities[8–10] and exposure to various environmental stressors.[11–13] One such environmental stressor of critical relevance in a rapidly warming world is heat stress. Urban areas are usually warmer than their surroundings, which, in combination with rising urban populations and interactions with global climate change, disproportionately exposes urban residents to extreme heat[14–16] and its health and economic impacts.[17,18] With increasing trends in regional heat waves,[19] and multiple severe heat waves in 2021 and 2022, there has been a push for

policy makers to implement urban heat response plans.[20] As cities develop these adaptation plans to extreme heat, it is crucial to understand the equity implications of these investments.

Given large urban heterogeneities, heat exposure is not likely to be equally distributed within cities. Research suggests a correlation between high temperatures and economically vulnerable neighborhoods, particularly in the US.[13,21–24] One obstacle to understanding the equity of the distribution of urban heat exposure has been the lack of urban-resolving datasets.[25] Human physiological response to heat—or heat stress—depends on, among other factors, air temperature (*Ta*) and relative humidity (RH).[26] Some studies have monitored one or more of these factors, but only for limited geographic areas for a limited extent of time.[27–29] They are thus unable to uncover systematic inequities in heat stress.

The standard approach for examining hotspots of heat exposure in multicity studies has been to use satellite-derived land surface temperature (LST) as a proxy for urban heat.[30,31] While this method has the advantage of allowing high-resolution equity analysis of the distribution of heat for multiple cities, LST is, at best, a crude proxy for heat stress. Not only does it ignore humidity, which is generally reduced by urbanization,[32,33] it does not measure ambient *Ta*. Urban LST is a consolidated two-dimensional estimate of the radiative skin temperature (*Tsk*) of the complex three-dimensional urban fabric[34] for clear-sky conditions during the satellite overpass. Thus, both LST and *Tsk* are fundamentally different from *Ta* and heat stress.[29,35,36] Numerical modeling can estimate factors responsible for heat stress at appropriate spatiotemporal scales within urban environments. Such modeling can be computationally burdensome, however, and the studies using this approach have either focused on a small number of cities[37] or used model resolutions that are too coarse to examine within-city heterogeneity.[33,38]

Urban environmental disparities depend on how the stressor and population groups (in terms of race and class) covary. Distributions in environmental stressors depend strongly on the urban physical environment and its heterogeneity. Built-up density leads to local warming, while the urban green infrastructure, such as parks or trees, cools the surroundings.[39,40] Vegetation also increases RH, however, which tends to increase heat stress, all else remaining equal.[28] For the most part, the directions of these physical associations are consistent across cities. A greater source of variability is how populations are distributed.[41] The demographic distribution of urban populations depends on various factors, from rules and regulations to presence or absence of certain features and services to wider social and cultural narratives.[42,43] The United States is a particularly interesting case due to well-documented patterns of urban population distributions and racial segregation seen in past and present cities.[9,44–46] With limited exceptions, US cities have often been characterized by the movement of richer and whiter populations to suburban areas, known as urban flight or white flight, with the urban core frequently populated by poorer and primarily non-white residents.[46,47] This present structure of US cities has frequently been linked to historic racism, including practices like "redlining."[45,48]

Due to the lack of heat stress estimates at fine scales, several recent studies have used satellite-derived LST to demonstrate pervasive disparities in potential heat exposure in US cities,[13,24,49–52] with poorer and primarily non-white neighborhoods showing higher LST values. The implications of using LST instead of *Ta* or more comprehensive physiologically metrics for urban heat exposure disparities have been discussed only in passing.[24,53] Since the impacts of urbanization on LST, *Tsk*, *Ta*, and RH can differ widely in magnitude,[36] it is critical to examine whether heat stress disparities are pervasive in the US, both to better understand potential risks to disadvantaged populations and for informing equitable urban design and policy.

Our results show income- and race-based disparities in heat stress to be pervasive within US cities, with roughly 94% of the US urban population (228 million people) living in cities where moist outdoor heat stress would burden the poor. Heat stress inequities between white and non-white urban populations are strongly associated with residential segregation, which is present to some extent in all 481 cities. Finally, historically redlined neighborhoods show the highest heat exposure (compared with other neighborhood grades) regardless of the metric of exposure used. Drawing from these results, we discuss how the magnitude of these disparities varies for physiologically relevant metrics of heat stress versus commonly used satellite-derived proxies of heat exposure.

RESULTS

Methods summary

We use urban-resolving numerical model simulations to examine disparities in average summer maximum *Tsk*, *Ta*, and moist heat stress metrics within US cities for all-sky conditions (with and without clouds). Our offline approach, which uses a land-surface model with urban canopy representation forced by downscaled atmospheric forcing, allows us to overcome computational limitations and estimate heat stress at a 1 km scale over the continental United States (CONUS). We consider two operational metrics of moist heat stress under shaded conditions, the heat index (HI), used by the US National Weather Service, and the Humidex, used by the Meteorological Service of Canada, both representing the human physiological response to combinations of *Ta* and RH. Combining these results with US census tract demographic data, we calculate disparities in heat stress by race and income group for all 481 urbanized areas within the CONUS, home to around 240 million people. To evaluate potential historical drivers of these disparities, we also overlay these data with maps for 171 cities with available spatial data for historically redlined neighborhoods (Figure 1A). Overall, unlike multiple previous estimates of potential disparities of heat exposure across cities and redlining grades that have used satellite-derived LST,[13,23,24,50–52] we primarily focus on equivalent disparities in outdoor moist heat stress, which have greater relevance for human thermal discomfort. See the experimental procedures for more details.

Intra-urban variability in heat exposure

We examined census-tract level distributions of variables relevant to heat exposure across 481 urbanized areas (cities henceforth; Figure 1A) in the CONUS for northern hemisphere summer (June-July-August) 2014 to 2018. These variables include LST derived from the moderate resolution imaging spectroradiometer (MODIS) sensor on board NASA's Aqua satellite after

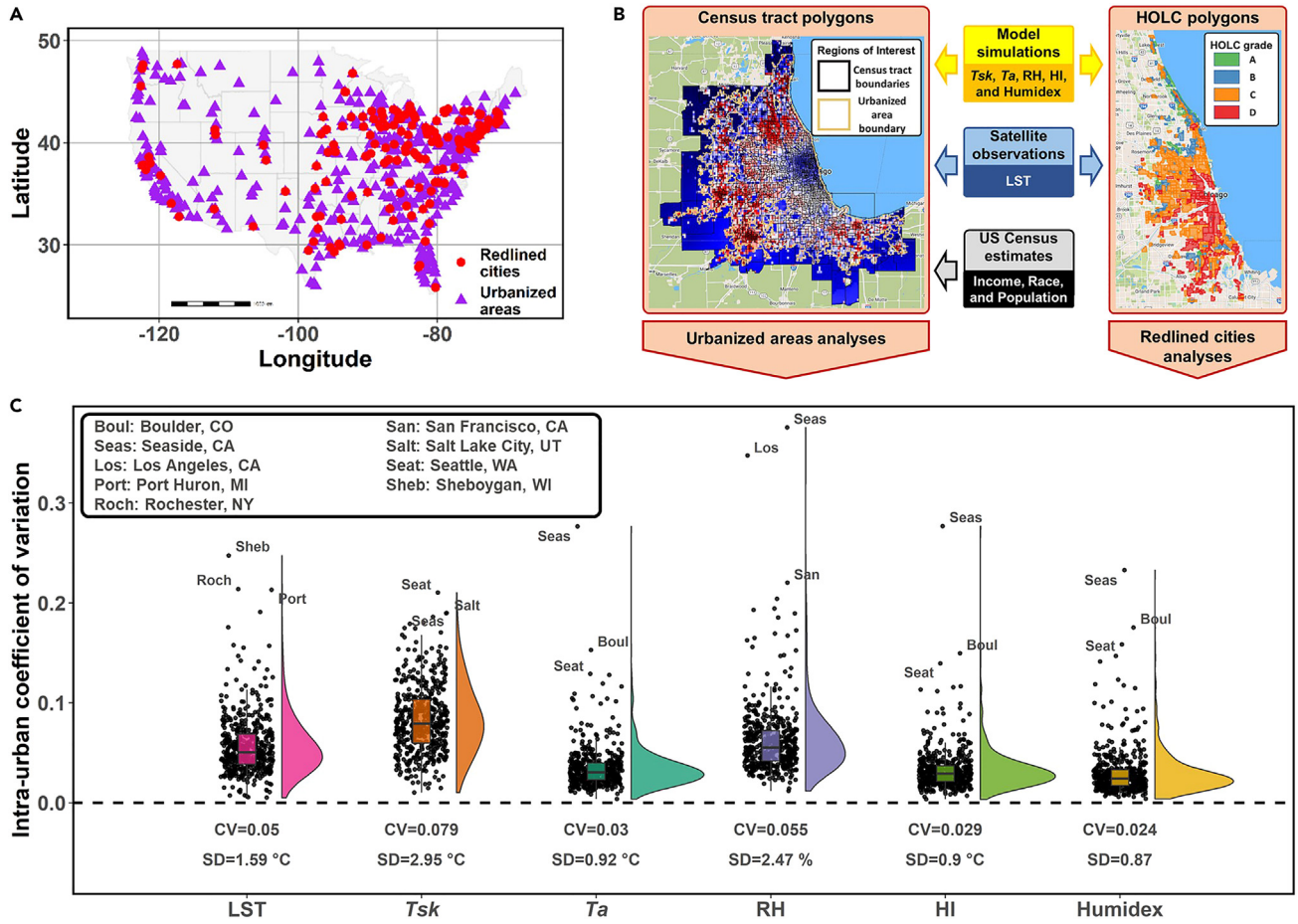

Figure 1. Study overview and intra-urban variability of heat exposure metrics

(A) The 481 urbanized areas and 171 redlined cities considered here.

(B) Study design, including data sources, variables of interest, and polygons used to disaggregate the data (using Chicago as an example). Here, the background colors in the census tract polygons box represent the spatial variability of average maximum summer air temperature. More information about the HOLC (Home Owners' Loan Corporation) polygons shown on the right can be found in the experimental procedures.

(C) Distributions of the CV of satellite-derived mean summer daytime LST and the average summer maximum of modeled *Tsk*, *Ta*, RH, HI, and Humidex across census tracts of the 481 urbanized areas. Median area-weighted SD and CV, as well as the three cities with the highest CV, are annotated for each variable.

pixel-level quality control (limiting LST uncertainty to less than 3°C; see experimental procedures) and modeled variables like *Tsk*, 2-m *Ta*, HI, and Humidex (Figure 1B).

The composite median of the standard deviation (σ) of the modeled variables across these 481 cities varies from 2.95°C for *Tsk* to 0.92°C for *Ta* to 0.87 for Humidex (Figure 1C). Since these variables have different means (μ) and units, we also checked the coefficient of variation (CV = $\frac{\sigma}{\mu}$), which is unitless and scale independent. Higher CV is seen for *Tsk* (0.079) and LST (0.05) than for *Ta* and HI (≈0.03 for each). Among the 481 cities, the CV is higher for *Tsk* (LST) than for HI and Humidex in ≈96% (91%) of cases. A city-scale example is shown for Chicago (Figures 1B and S1), which was the center of the well-documented 1995 heat wave.[54] Temperatures peak at the urban center compared with the cooler rural outskirts, with *Tsk* and LST showing higher intra-urban variability than *Ta*. In fact, *Ta* shows a slight decrease near the lakeshore, which is expected, due to the impact of lake breeze during daytime.[55] In parallel, the RH is lower in the warmer parts of the city, generally increasing toward the suburbs (Figure S1D). Although lower RH partially offsets the effect of higher *Ta* on heat stress, overall heat stress (HI and Humidex) remains higher in the urban core (Figures S1E and S1F).

Income inequality and heat-related disparities

To examine income-based disparities in heat exposure, we first calculated the statistical associations between census-tract-level median per capita income and the different heat exposure metrics for each of the 481 cities (comprising 54,684 census tracts). Here, linear models were first used to examine these associations for their easier interpretability and in line with previous studies on environmental disparities.[50,53,56] The correlations were negative in almost all cases (90.6% for LST and ≈92% for *Tsk* and *Ta*), i.e., poorer urban residents live in hotter areas (Figures 2A–2C). Wealthier populations live in more humid neighborhoods than poorer populations, with RH positively correlated

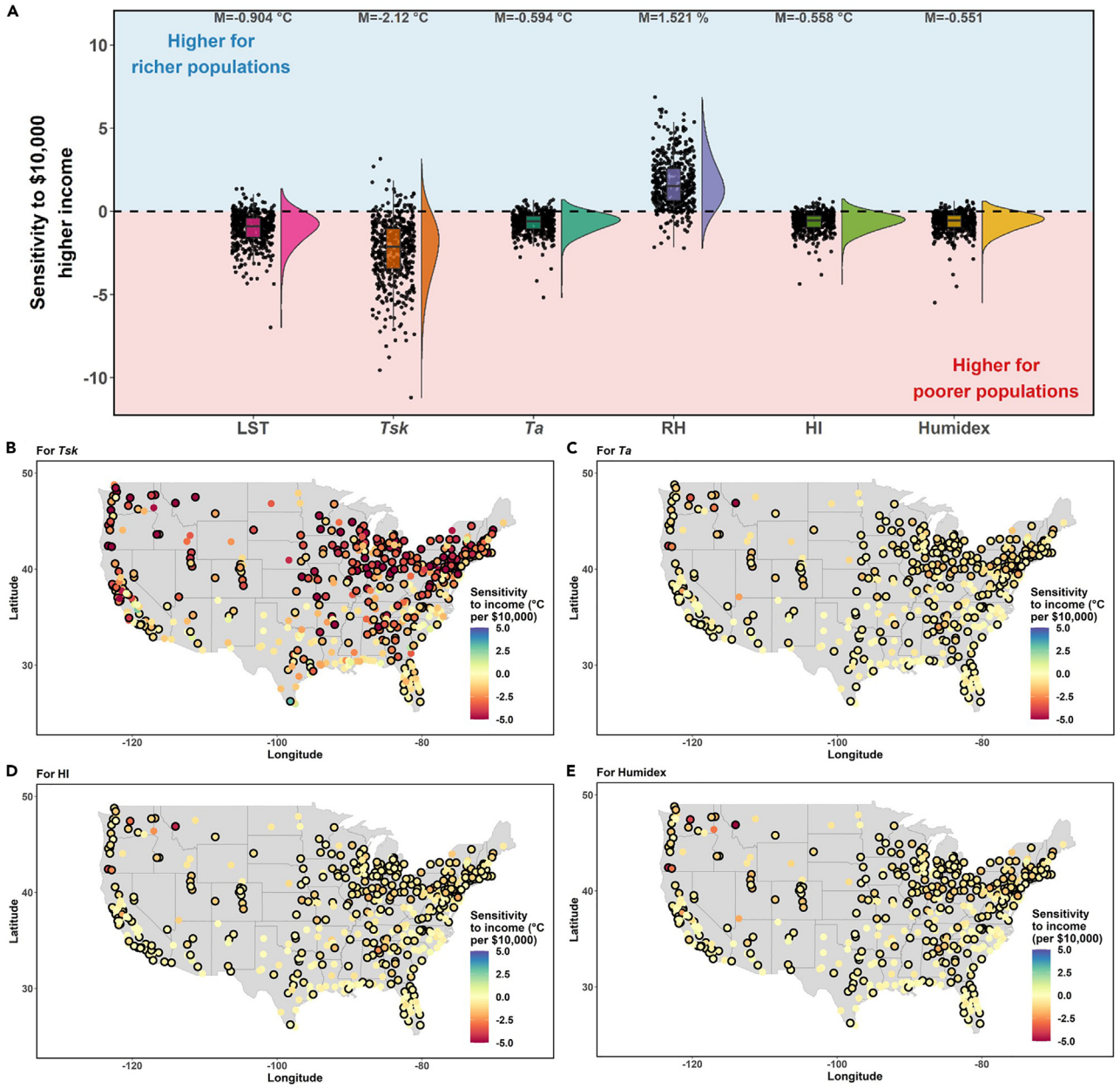

Figure 2. Disparities in heat exposure metrics by income

(A) Distributions of slopes of satellite-derived mean summer daytime LST and the average summer maximum of modeled *Tsk*, *Ta*, RH, HI, and Humidex with income across the 481 cities (median slope for each variable is annotated).

(B–E) The spatial distributions of the slopes of the linear regressions between income and (B) *Tsk*, (C) *Ta*, (D) HI, and (E) Humidex. Circles with black outlines represent statistically significant correlations ($p < 0.01$).

with income in 91.9% of cases, with 54.5% of these positively correlated cases being statistically significant ($p < 0.01$). Higher temperature is more important than lower humidity for heat stress in poorer neighborhoods, with negative correlations of income with HI and Humidex in ≈93% of cases (Figures 2A, 2D, and 2E). Linear regressions estimate median changes in heat exposure per $10,000 greater income of −0.91°C, −2.12°C, −0.59°C, 1.52%, −0.56°C, and −0.55 for LST, *Tsk*, *Ta*, RH, HI, and Humidex, respectively. In ≈91% (~77%) of these cites, HI and Humidex are less sensitive to income than *Tsk* (LST). This analysis shows pervasive income-based disparities in heat exposure and heat stress metrics in most US cities.

We also examined associations between income inequality and distributional inequity in outdoor HI across cities. Unitless metrics of income inequality (Gini coefficient) and HI inequity (modified environmental concentration index) were used for this purpose to allow easy comparison between cities. Overall,

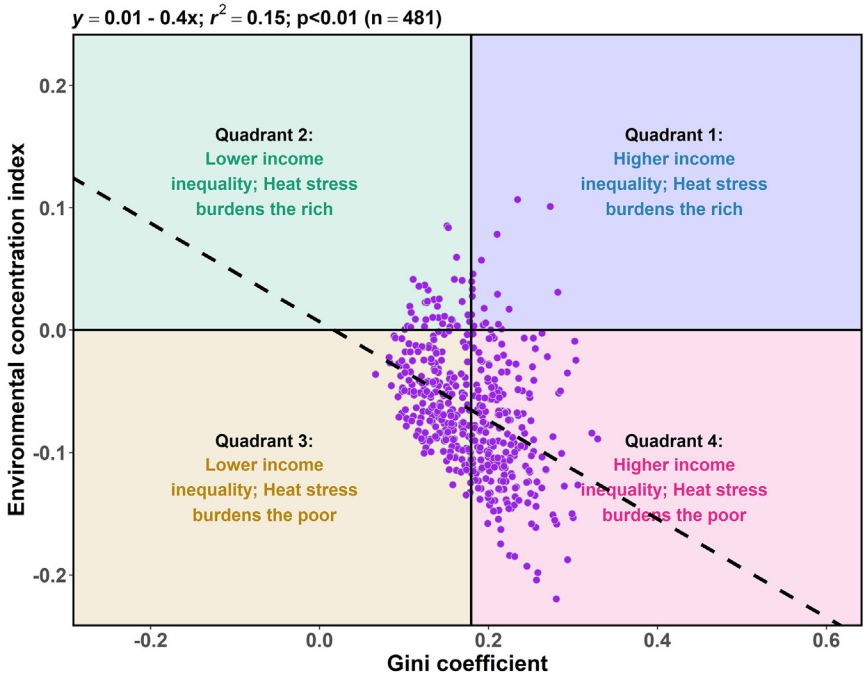

Figure 3. City typologies demonstrating income and heat stress inequalities

Four-quadrant plot of heat stress (HI) concentration index (based on income) and Gini coefficient for the 481 cities considered here. The quadrant threshold for income inequality is the mean Gini coefficient of the sample (0.18), and the quadrant threshold for heat stress distributional inequity is 0. The line of best fit between city-level heat stress concentration index and Gini coefficient and the associated linear regression equation, coefficient of determination (r^2), p value, and sample size (n) are noted.

a moderate negative correlation (r^2 = 0.15) is seen between the Gini coefficient and the environmental concentration index for HI, i.e., cities with higher income inequalities are associated with higher disparities in HI. We consequently placed the 481 cities into one of four typologies representing combinations of income inequality and distributional inequity in outdoor HI (Figure 3). The largest percentage of these cities (46%; 221 of 481) fall into the bottom right quadrant (quadrant 4), with higher-than-average income inequality and HI burdening the poor. These cities, including some of the largest and most populated ones (New York, Los Angeles, Chicago, Philadelphia, etc.), have the potential to compound existing inequalities through unequal exposure to environmental stressors. The second largest typology of cities is those in the bottom left quadrant (quadrant 3), with relativity lower income inequality compared with the mean of the sample and HI still burdening the poor. Combined, these two quadrants cover almost 89% (427) of the cities and close to 94% (228 million) of the US urban population. The two upper quadrants (quadrants 1 and 2), where HI burdens the rich comprise only 43 cities and around 6% of the population (Figure 2). The highest Gini coefficient is seen for Indio in California (0.33), followed by Los Angeles (0.32) and New York (0.31), while the lowest Gini is for Cartersville, Georgia (0.07). The highest concentration index for HI is for McAllen, Texas (0.11), with the lowest being for State College, Philadelphia (−0.22).

Residential segregation and heat-related disparities

Correlating heat exposure metrics with race showed similar widespread disparities. In ≈90.5% of cases (91.9% for LST; Figure S2B), HI and Humidex (Figures 4B and 4D) are negatively associated with the percentage of white population of the census tracts. In contrast, in ≈87.5% of the cities, census tracts with higher percentage black populations have higher *Tsk*, *Ta*, HI, and Humidex than those with lower percentage black populations (Figures 4A, S2C, 4C, and S2E). The median sensitivity of *Tsk* and LST to higher percentage white population is −0.13°C and −0.06°C, respectively, which decreases to approximately −0.04°C for *Ta* and HI and approximately −0.03 for Humidex. The median census-tract-scale *Tsk* (LST) is greater by 0.15°C (0.07°C) per percentage higher black population, but only about 0.04°C greater for *Ta* and HI. All races other than white show positive correlations with LST, *Tsk*, *Ta*, HI, and Humidex (Figure S3).

We examined associations between present-day housing segregation and heat stress inequities by calculating a dissimilarity index between white and non-white populations for each city and the corresponding concentration index based on proportion of white residents. We see a strong correlation (r^2 = 0.47) between residential segregation and race-based outdoor HI inequities (Figure 5). Placing cities into typologies as done earlier for income-based inequities, the largest percentage of these cities (44%; 213 of 481) fall into the bottom left quadrant (quadrant 3), with lower-than-average residential segregation and HI burdening non-white residents. The second largest group is in quadrant 4 (212 of 481 or 44%), with HI burdening non-white residents and residential segregation being higher than the average. Overall, around 83% (57.8 million) of non-white US urban residents live in cities where HI burdens non-white populations.

Although traditionally one of the more common metrics of segregation,[57] a limitation of the dissimilarity index is that it is insensitive to the redistribution of minority populations among the census tracts that are above or below the reference distribution of the city.[58] Thus, the magnitude of segregation as measured by the dissimilarity index would change only when the minority populations (whether white or non-white) were moved from census tracts that have an overrepresentation of that minority (compared with the city average) to those that have an underrepresentation of that minority group. So, we considered two other metrics of segregation to confirm our results. One common way to measure segregation that avoids the limitation of the dissimilarity index is to use a Gini coefficient, as for income in the previous sub-section, but replacing income with proportion of white residents when computing the Lorenz and concentration curve (see experimental procedures). Another

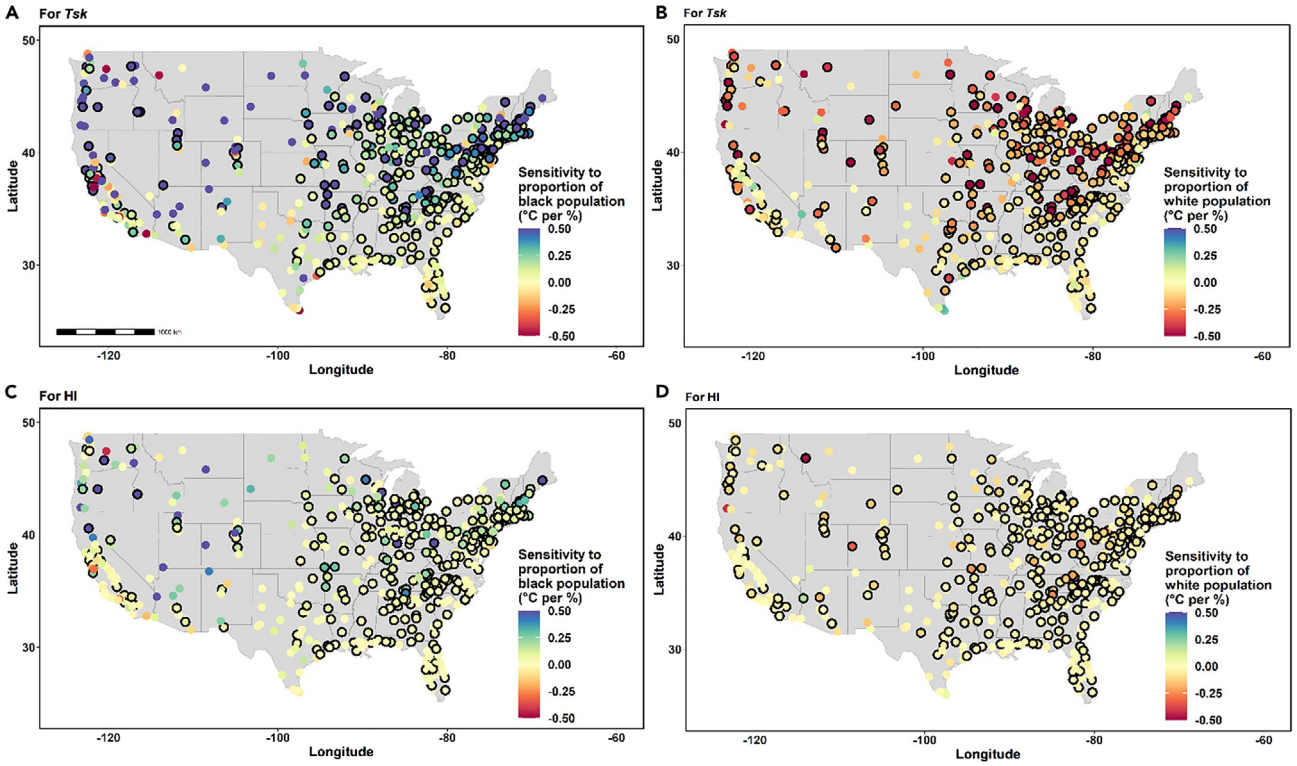

Figure 4. Disparities in heat exposure metrics by race

(A and C) The spatial distributions of the slopes of the linear regressions between the proportion of black population in a census tract and the average summer maximum of modeled *Tsk* and HI, respectively for the 481 cities.

(B and D) Similar to (A) and (C), but for the proportion of white population. Circles with black outlines represent statistically significant correlations ($p < 0.01$).

index that has recently become popular in the study of racial segregation[59] is Thiel's entropy index,[60] which measures the extent to which groups (in this case, white and non-white populations) are evenly distributed among sub-units of aggregation (in this case, census tracts). The Gini coefficient and Theil's entropy index, like the dissimilarity index, also vary between 0 and 1, but are sensitive to any redistribution of population groups. Even though there are some differences in the degree of associations (in terms of r^2 and slope) using these alternative measures of segregation (Figure S4), we can see that cities with higher residential segregation tend to show higher heat stress inequities in the United States.

Historical redlining and heat-related disparities

As also seen above, current heat exposure disparities depend on neighborhood-scale characteristics and urban population distributions.[24,50,53] In the United States, poorer and predominantly non-white neighborhoods tend to have less vegetation cover,[51,53,61] which influences local-scale temperatures.[39,40] Populations in and around US cities are distributed such that poorer populations generally live in urban centers.[47] Wealthier, white populations tend to be in the suburbs,[9,44] where there is more space for non-built-up land cover, including vegetation (i.e., building density is higher in poorer neighborhoods[62]).

Historical policies have impacts on contemporary environmental conditions.[7] For instance, the practice of redlining in the 1930s by the US federal government's Home Owners' Loan Corporation (HOLC) graded neighborhoods based on suitability of real estate investments. This security rating was largely based on the racial makeup of the neighborhood, with limited access to mortgage lending for poorer and minority populations, and has been shown to be associated with contemporary environmental conditions, although there are exceptions to this general tendency.[7,12,13,45,63,64]

To examine the associations between redlining and these disparities, we calculated anomalies for different metrics of heat exposure during the study period (Equation 4 in experimental procedures) for cities (n = 171) with all four security ratings. A total of 8,512 neighborhoods were considered in this analysis. The A- or "best"-rated neighborhoods have negative anomalies (less heat exposure than the area-wide mean) for all variables, and the D-rated or "hazardous" redlined neighborhoods show positive anomalies (Figures 6 and S6). Among the modeled variables, the difference in median anomalies (M) between the A- and the D-rated neighborhoods is higher for *Tsk* and LST than for *Ta*, HI, and Humidex. It is evident that historically redlined neighborhoods show higher heat exposure than their non-redlined counterparts. However, a broader question is how redlining is associated with the heat exposure disparities of the city as a whole, given the presence of segregation in US cities even before the practice.[46] To address this question, we re-examined associations between heat exposure and income after isolating all the

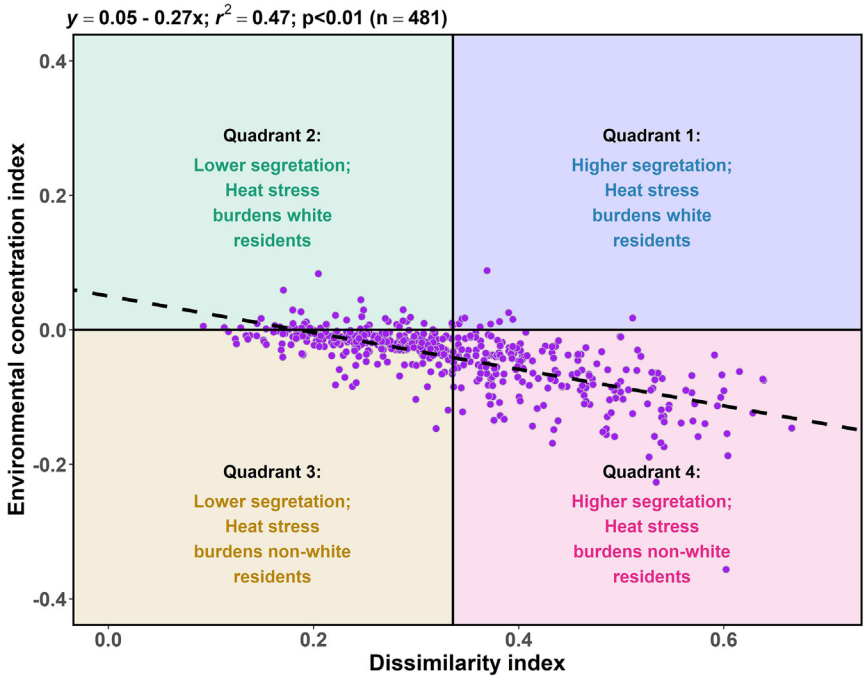

Figure 5. City typologies for residential segregation and heat stress inequalities

Four-quadrant plot of heat stress (HI) concentration index (based on proportion of white residents) and dissimilarity index for the 481 cities considered here. The quadrant threshold for residential segregation is the mean dissimilarity index of the sample (0.33), and the quadrant threshold for heat stress distributional inequity is 0. The line of best fit between city-level heat stress concentration index and dissimilarity index and the associated linear regression equation, coefficient of determination (r^2), p value, and sample size (n) are noted.

cities (urbanized areas) that overlapped with any redlined neighborhood. Of the 481 cities, 143 overlapped with the HOLC polygons, while the other 338 did not. These 143 cities form a smaller subset than the total number of cities (171) used in the previous analysis, since some of these urbanized areas cover multiple neighborhood groups.

Although income-based disparities in heat exposure metrics are seen for both groups (Figure S7), the cities that did not overlap with the HOLC polygons have a lower median correlation coefficient (r = 0.39 versus 0.43 for Humidex). While this result suggests that cities with previously redlined neighborhoods show a higher likelihood of present-day heat stress disparities than cities with no such redlining data (98% versus 91%), we should be careful about the interpretation of these results to claim that redlining was the cause behind these differences. This is because this analysis cannot be a true counterfactual scenario of no redlining, both because the redlining data may not be comprehensive and because redlining policies may have shaped urban development elsewhere in the country.[45]

DISCUSSION

It is important to stress that all models have limitations, with especially large uncertainties when simulating urban-scale processes and variables. For instance, in our original model outputs, the mean bias error of urbanized area average *Ta* compared with an independent dataset was 5.74°C, which was reduced to 1.93°C after bias correcting the dataset using a network of ground-based weather stations. In this article, we focus on the results after bias correction due to the higher accuracy, but more details about the bias-correction process, model evaluation, and model uncertainties are given in the experimental procedures and Note S1. The results of the study should be interpreted keeping these uncertainties in mind. Overall, our high-resolution CONUS-wide modeling demonstrates pervasive disparities in average summertime maximum *Ta* and heat stress in US cities both before (not shown) and after bias correction. These results have important implications for urban heat exposure and corresponding public health consequences on vulnerable populations. For instance, using heat exposure anomalies for each census tract relative to its city, a white urban resident in the United States is exposed to an average *Ta* anomaly of −0.22°C, while a black person is exposed to 0.28°C. Similarly, the HI anomalies deviate slightly less between white (−0.21°C) and black (0.28°C) residents. For anomalies in Humidex, the deviation between white and black residents is slightly lower (−0.20 and 0.26, respectively) than for *Ta* and HI. In comparison, if satellite-derived LST were used to calculate these disparities, the anomalies would be much higher (−0.47°C and 0.73°C for the average white and black resident, respectively).

Across cities, HI inequities are associated moderately with income inequality (Gini coefficient; Figure 3) and strongly with race-based residential segregation (dissimilarity index, Gini coefficient for race, and Theil's entropy index; Figures 5 and S4). Similarly, historical residential segregation (redlining) still demonstrates a noticeable association with heat-related exposure in present-day cities regardless of the metric used. These associations are seen both from anomalies in heat exposure metrics across redlining grades and when comparing cities with and without any redlined neighborhood (Figures 6, S6, and S7). It is important to stress here that the marginal benefit of a unit reduction in summer daytime heat exposure is lower than the marginal adverse health impacts of a unit heat exposure increase due to the nonlinear impacts of temperature on health.[24] As such, the assumptions of linearity made between heat exposure metrics and socioeconomic characteristics would underestimate the actual health impacts, especially at finer spatiotemporal scales. This risk is further compounded by higher vulnerability in poorer populations, who frequently lack the resources (such as household air conditioning) to cope during extreme heat events.[54]

Satellite-derived LST has been widely used as a proxy for urban heat exposure and its potential disparities due to the lack of *in situ Ta* and RH observations at the same scale.[29,36] Here, we show that, for cities in the United States, these disparities are pervasive regardless of the metric used. However, this finding

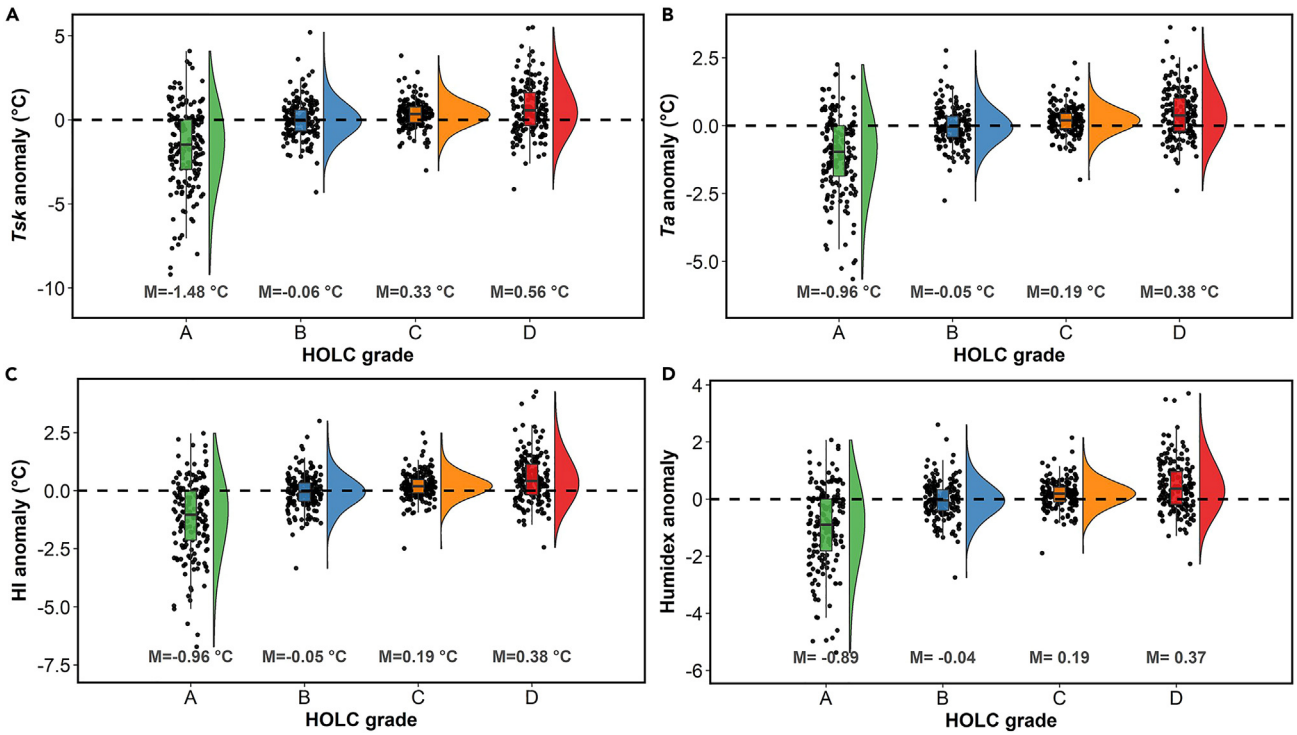

Figure 6. Temperature anomalies by HOLC security rating

The distributions of anomalies in average summer maximum of modeled (A) *Tsk*, (B) *Ta*, (C) HI, and (D) Humidex across 171 redlined cities. The numbers at the bottom give median anomalies for each group. Here, A is "best" HOLC security rating, B is "still desirable," C is "definitely declining," and D is "hazardous."

is true only for the direction of the disparities (i.e., heat stress is higher in census tracts with poorer and non-white populations), but not for the magnitude. The differences in the magnitudes are seen for disparities both by income and race and given by the weaker sensitivities for *Ta*, HI, and Humidex to socioeconomic variables than for *Tsk* (Figures 3 and 4). Similarly, anomalies for LST are generally more extreme for all population groups than for *Ta*, HI, or Humidex, suggesting that satellites overestimate disparities in heat exposure. This overestimation of disparities when using LST instead of *Ta* is both suggested by comparing the simulated variables and the satellite observations (Figure 2A) and seen when examining disparities in average maximum summertime *Ta* using a newly developed gridded near-surface *Ta* dataset (Figure S8), with the added caveat that this dataset is based on a statistical model,[65] not a process-based model as implemented here. Finally, solar insolation and wind speed, which we do not focus on, can provide a more complete picture of human physiological response to heat,[15,29,66] but are rarely measured within cities and difficult to model at appropriate scales to emulate human environmental exposure. As such, we suggest caution when relying on satellite-derived quantitative estimates alone for heat-related policy making and urban planning and call for more *in situ* observations[25,35] and further urban model development to accurately quantify these environmental disparities.

While it is evident from these model simulations that outdoor moist heat stress disparities are pervasive across US cities, a broader question is how to protect vulnerable populations from these environmental heat extremes. In the environmental equity literature, heat exposure disparities have been frequently studied in conjunction with distributional inequities in green space.[12,51] This makes sense, since urban vegetation reduces local temperature through evaporative cooling and trees also reduce sun exposure through shading.[40,67] With the intent of reducing heat stress disparities, however, a few things need to be considered. First, poor and densely populated urban cores have limited space for planting trees, constraining potential for vegetation-mediated cooling.[62,68] Second, many quantitative estimates of the cooling potential of vegetation over large spatial extents come from satellite-derived LST.[39,68] Satellites provide only the radiative temperature of the top of the canopy, and the impact of vegetation on *Ta* and heat stress can be quite different.[28,36] Third, and probably most important, it is unknown how feasible urban greening is to address heat-related inequities over longer time frames. In the United States, green neighborhoods tend to hold a real estate premium, and "green gentrification" may price out poorer populations over time.[69] As such, parallel regulations may be needed to ensure that the intended beneficiaries of heat stress mitigation strategies in disadvantaged neighborhoods can continue to live there.[23,70] Moreover, we need to better understand behavioral response to neighborhood-scale heat mitigation strategies beyond urban greening, such as white roofs, green roofs, reflective pavements, etc. These strategies may show different marginal willingness to pay than that for neighborhood green spaces, and can often be more effective at heat mitigation.[71,72] Since the

consequences of heat extremes go beyond health, with adverse outcomes for labor productivity and economic growth,[18,73] there is a critical need to develop policy tools to equitably address urban heat stress as we prepare for future heat extremes on a more urbanized planet.

EXPERIMENTAL PROCEDURES

Resource availability

Lead contact

Further information and requests for resources and materials should be directed to and will be fulfilled by the lead contact, TC Chakraborty (tc.chakraborty@pnnl.gov).

Materials availability

Materials generated in this study have been deposited in Mendeley Data: https://www.doi.org/10.17632/jgv5hmzc44.1.

Data and code availability

All data and code required to generate the census tract and HOLC polygon level heat stress indices, as well as the urban-scale segregation indices, have been deposited in Mendeley Data: https://www.doi.org/10.17632/jgv5hmzc44.1.

Regions of interest

Two sets of regions of interest were used in the present study (Figures 1A and 1B). First, we extracted all census tracts overlapping (not necessarily fully contained in) the US Census Bureau's urbanized areas dataset.[74] This included 497 polygons with populations exceeding 50,000. Of these, 481 are within the CONUS region, the extent of the modeled dataset described in the next sub-section. The final 54,684 overlapping census tracts were grouped by urbanized area (n = 481). Socioeconomic information like race, income, and population were extracted from the 5-year 2017 American Community Survey.[75] The race categories are consistent with the classification used by the US Census Bureau. Our analysis covered census tracts that house around 240 million people, over 70% of the total US population.

The second set of regions comprised neighborhood polygons (example for Chicago in Figure 1B) corresponding to security ratings given by the US federal government's HOLC in the 1930s and digitized by the University of Richmond's Digital Scholarship Lab.[48] This practice, called redlining, graded neighborhoods based on suitability of real estate investments. This security rating was largely based on the racial makeup of the neighborhood, with limited access to mortgage lending for poorer and minority populations, and has had consequences for disparities in heat exposure and access to green spaces in present-day cities.[12,13] Of the 196 cities included in the dataset, we used only the 171 that have all four grades of neighborhood rating: A being "best," B being "still desirable," C being "definitely declining," and D being "hazardous."

Model simulations and bias correction

The High-Resolution Land Data Assimilation System (HRLDAS)[76] is an offline (one-way coupled) system used to estimate near-surface meteorology. It allows for use of historical observed meteorology, in this case the National Land Data Assimilation System Phase-2 (NLDAS-2),[77] and high-resolution land-cover data (the National Land Cover Database here, https://www.usgs.gov/centers/eros/science/national-land-cover-database) to drive the land-surface model components within the Weather Research and Forecasting (WRF) atmospheric model[78] in a one-dimensional column mode neglecting lateral advection and solving the full three-dimensional atmospheric time-stepping equations. The low computational cost and strong constraints of using observed meteorology in an offline system make HRLDAS useful for many applications needing gridded surface meteorological data, including examination of urban heat islands.[79] More details are provided in the community repository for access and contributions (https://github.com/NCAR/hrldas). Here, we use the state-of-the-science Noah-MP[80] land-surface model and a single-layer urban canopy model[81] to simulate near-surface (2 m) *Ta* and specific humidity (*q2*) using a 1 km horizontal resolution grid and an hourly timestep over CONUS. The urban canopy model divides the urban geometry into three surface types, namely, roof, wall, and road, and simulates the exchange of energy and momentum between the urban surface and the atmosphere. It also parameterizes the influence of urban canyons, including building shadows and reflected radiation on surface climate. Urban land-cover type and urban fraction are modified annually in the model between 2014 and 2018 using linear trends estimated from the National Land Cover Database[82] for the years 2011, 2016, and 2019.

The original model simulations show overestimations in urbanized area average *Ta* compared with estimates from the Daymet version 4 dataset[83] (Figure S5A). While some overestimation is expected, since Daymet does not accurately represent urban microclimates due to the dearth of assimilated urban observations,[84] a mean bias error (MBE) of 5.74°C is still unreasonably high. So, we performed a bias correction exercise to the raw maximum and minimum daily *Ta* independently using all available station data that pass quality control checks in the Global Historical Climatology Network Daily (GHCNd),[85] the Meteorological Assimilation Data Ingest System (MADIS, https://madis.noaa.gov), and monthly maximum/minimum value checks within our workflow.

The GHCNd dataset contains maximum and minimum *Ta*. We used the surface Mesonet station data within MADIS and computed the daily maximum *Ta* and minimum *Ta* directly from their native high temporal resolution observations. Then, for each day and grid point with a station, we found up to 20 valid stations within 500 km of that grid point and estimated the temperature bias for the simplified land-cover type (non-urban or urban). Valid station observations were adjusted to the grid box elevation using the mean lapse rate of all station-grid combinations and the specific station-grid point elevation difference. Use of the mean lapse rate reduces noise in the estimated lapse rate due to measurement uncertainty. We then estimated the temperature bias using a 3 × 3 grid box (9 km^2) average of the raw HRLDAS output and the distance weighted temperature average of all valid stations with the same land-cover classification (non-urban or urban) as the target grid point. Urban and non-urban bias estimates were then weighted by urban fraction for each grid cell and added to the raw maximum and minimum *Ta* values. We did not bias correct *q2* due to the dearth of available *q2* measurements. Overall, after bias correction, the dataset performed much better compared with the Daymet estimates, in terms of capturing both variability and magnitude (Figure S5B). The small positive MBE was expected, since our dataset explicitly resolved the urban signal, since it is estimated by the single-layer urban canopy model, unlike Daymet. The direction of the within-city variability in Daymet is captured by the model in 76% of cases, which rises to almost 80% after bias correction. So while there are observational deficiencies that prevented an apples-to-apples comparison at these scales over cities, we are relatively confident about the direction of the within-city variability in our dataset, which is strongly associated with the likelihood of urban heat stress disparities.

Estimating outdoor moist heat stress

We processed data for 5 years (2014–2018) of Northern Hemisphere summer months (June, July, and August) to represent present-day all-sky conditions. We used daily maximum and minimum *Tsk*, *Ta*, and *q2* to generate census-tract-level average summer maximum and minimum through first temporal (taking average of all daily maxima and minima) and then spatial (taking average of these temporal averages for all grids overlaying each census tract) averaging. Average summer minimum RH was estimated from the maximum *Ta* and minimum *q2* (also see Note S1 for results from upper bound estimates). In addition to *Tsk* and *Ta*, we calculated the average summer maximum of apparent temperature or HI using US National Weather Service methodology.[86] The main equation is:

$$\begin{aligned} HI = & -42.379 + 2.04901523Ta + 10.14333127RH - 0.22475541TaRH \\ & - 6.83783 \times 10^{-3} Ta^2 - 5.481717 \times 10^{-2} RH^2 \\ & + 1.22874 \times 10^{-3} Ta^2 RH + 8.5282 \times 10^{-4} TaRH^2 \\ & - 1.99 \times 10^{-6} Ta^2 RH^2. \end{aligned} \quad \text{(Equation 1)}$$

In Equation 1, *Ta* in °F (average maximum values) and RH in % (based on average minimum values of *q2*; see Note S1) are used, and adjustments are made based on different ranges of RH and *Ta*.[86] When the average of HI and *Ta* is less than 80°F, the following simple equation (Equation 2) is used:

$$HI = 0.5 \times [Ta + 61 + [(Ta - 68) \times 1.2] + (0.094RH)]. \quad \text{(Equation 2)}$$

Since the HI formulation above is strongly temperature sensitive,[66] we also calculated a second operational metric used by the Meteorological Service of Canada, the Humidex. This is given by Equation 3:

$$Humidex = Ta + 0.5555 \times \left(6.11 \times e^{5417.753 \times \left(\frac{1}{273.16} - \frac{1}{273.15+Td}\right)} - 10\right), \quad \text{(Equation 3)}$$

where *Td* is the dewpoint temperature calculated from maximum *Ta* and minimum RH.

Satellite data

Satellite-derived LST was used as a reference to contextualize the results within the recent studies that have examined disparities in heat exposure in US cities.[24,50,51,53] We processed daily daytime LST images corresponding to around 1:30 p.m. local time for summer derived from the MODIS sensor[87] on board the Aqua satellite for the years of model simulations considered (2014–2018). Pixel-level quality control flags were used to choose only data that have an uncertainty of less than 3°C, which minimizes errors from cloud interference. Summer daytime composites were generated with all available data, and spatial means were calculated corresponding to all census tracts and HOLC neighborhoods. This standard method of spatial aggregation uses weighted reducers that consider the fractional area of each pixel within the region as weights before calculating statistical summaries. Note that we used MODIS-derived LST for reference (Figure S6A) to keep it consistent with the other analyses on urbanized areas. Hoffman et al.[13] used Landsat satellite-derived LST. For comparison with that study, we also calculated the HOLC neighborhood-level LST from the Landsat 8 satellite[88] for the same period. The statistical mono-window algorithm[89] was used to calculate LST from top-of-atmosphere thermal radiance measured by Landsat. This algorithm includes surface emissivity prescription based on remotely sensed fractional vegetation estimates and removal of data contaminated by clouds or cloud shadows using pixel-level quality control flags. Landsat is different from MODIS Aqua in several ways (Note S1) and shows a greater variability in LST anomalies (Figure S6B). The higher urban LST signal from Landsat observations is also seen when comparing against estimates from MODIS Terra, which has an overpass time similar to that of Landsat.[90] All satellite data, as well as the summertime composites from the model simulations, were processed on the Google Earth Engine platform.[89]

Data processing and analysis

Different variables were used for satellite-derived LST and modeled *Tsk* because *Tsk* is not dependent on a two-dimensional view of a three-dimensional urban surface like LST.[34] Note that the MODIS LST is mainly meant to provide only a reference, since it is commonly used in multicity studies.[24,31,50] However, the main variables of interest are maximum *Tsk*, *Ta*, HI, and Humidex, since they are all constrained by the same process-based modeling framework and the assumptions therein. For our model simulations, *Tsk* is the area-weighted radiometric skin temperature of all building walls, roofs, and roads within the built-up grids. Due to the surface heterogeneity of cities, we suggest caution when comparing satellite-derived LST and modeled *Tsk* over individual grids. Moreover, LST is only for clear-sky conditions at the satellite overpass time (not necessarily when LST is highest), while the modeled *Tsk* is available for cloudy days and can resolve the daily maxima (Note S1). Despite these differences, we would still expect LST and *Tsk* to show similar overall patterns within cities using census-tract-wide spatial means due to the strong constraints provided by local surface properties on radiative temperature. We found that the *Tsk* from our modeling framework generally captured the intra-urban variability in LST (Figure S9A), with positive correlation coefficients between the two in all but five of the urbanized areas and coefficients higher than 0.8 in 65% of cases. However, *Tsk* generally showed more variability than LST (see Figure S1 for Chicago example and Figure S8B for summary), with the slopes of the linear regression being greater than 1 in 88% of cases and greater than 2 in 28% of cases. This could partially be due to the lack of an advection scheme in the uncoupled model simulations, which would normally mediate intra-urban variability, and also due to the differences in the satellite overpass time and the daily maxima. Note, however, that the model does receive the spatial variability from the HRLDAS forcing. Moreover, the bias correction of *Ta* using observational constraints further improved our estimates. Figures 1A and 1B show overviews of the data sources, variables of interest, and geographic agglomerations used in the present study.

Unless otherwise noted, all analyses, including computations of the standard deviation (SD) of the variables within cities and the validations above, were done using census-tract-level information. Since the different variables do not have the same range, to better compare the intra-urban variability, the CV ($=\frac{\sigma}{\mu}$) was also calculated. Note that we calculated the CV of all temperature metrics after first converting the values to K, since it is not appropriate to examine the CV of a variable expressed in an interval scale like °C. Data for each of the grouped census tracts corresponding to the 481 urbanized areas were used to check linear correlations between the variables (LST, *Tsk*, *Ta*, RH, HI, and Humidex) and the socioeconomic estimates, like income and percentage of the census-tract population of each race. To account for the impact of the different range of values on the slopes of the linear regressions, we also standardized the variables (force to range between 0 and 1) for comparison (Figure S10). Unlike the use of unitless inequality indices to examine urban typologies (see next sub-section), this statistical analysis provided the sensitivity of heat exposure to neighborhood socioeconomic characteristics in physically interpretable units.

For the HOLC polygons, grade-level anomalies were calculated from the average value for the city following Hoffman et al.[13] For instance, the *Tsk* anomaly for D-rated neighborhoods is given by Equation 4:

$$\Delta Tsk = Tsk_D - Tsk_{av}, \quad \text{(Equation 4)}$$

where Tsk_D is the skin temperature for the D-rated neighborhoods and Tsk_{av} is the average *Tsk* of all neighborhoods of a city.

Similar anomalies were also calculated for census-tract-level variables against their corresponding urbanized areas to compare population-weighted heat exposures. As an example, the *Ta* anomaly for census tract is given by:

$$\Delta Ta = Ta_t - Ta_u, \quad \text{(Equation 5)}$$

where Ta_t is the air temperature for a census tract and Ta_u is the average *Ta* of the urbanized area. These anomalies are important to account for the large variability in the background temperatures of cities throughout the United States.

The 1 km resolution of both the simulated variables and the MODIS observations is finer than ~84% of the census tracts used in the study and thus can resolve the general spatial distribution of the variables within the urbanized areas. However, this resolution is finer than only ~44% of the HOLC-graded polygons. As such, we suggest caution when examining the anomalies for individual neighborhoods, although the comparison of the magnitude of the anomalies across variables is still useful since they are all at the same resolution.

Generating city typologies using inequality metrics

In addition to the statistical analyses, we provided unit-free representations of inequalities in income and distributional inequities in outdoor HI using methods from welfare economics.[91] These representations were used to bin each of the 481 cities into one of four typologies (Figure 2) representing combinations of income inequality and HI inequities. City-scale summaries of income inequality are given by the Gini coefficient (*G*), formulated as:

$$G = 1 - 2\int_0^1 L(X)dX. \quad \text{(Equation 6)}$$

In Equation 6, the function $L(X)$ represents the Lorenz curve, a graphical relationship between cumulative population and the cumulative income by the said population ranked from the poorest to the richest,[92] for the city. The closer the Lorenz curve is to a 45° line, the more equal is the distribution of income, and the Gini coefficient (Equation 6) approaches 0. Higher Gini coefficients represent higher inequality, with an upper bound of 1. Although Gini coefficients are always positive (i.e., all cities have income inequality), we used the mean Gini coefficient of the 481 cities as a threshold between lower than and higher than average income inequality for grouping the cities into the typologies.

For summarizing heat exposure disparities, we used the environmental concentration index (*CI*), given by:

$$CI = 1 - 2\int_0^1 H(X)dX. \quad \text{(Equation 7)}$$

Similar to the Lorenz curve, the function $H(X)$ in Equation 7 represents the concentration curve, the relationship between cumulative population and distribution of a variable (in this case, heat exposure metrics) for that population ranked by income.[93] The concentration curve can cross the 45° line, since variables other than income can have both pro-poor and pro-rich distributions. Thus, the *CI* can vary from −1 to 1. Since higher heat stress is an undesirable outcome, negative *CI* values indicate pro-rich distributions (primary burden on the poor) and positive values represent pro-poor distributions (primary burden on the rich). The *CI* value of 0 represents completely non-biased distribution and is the threshold used for separating heat stress distribution inequities into pro-poor and pro-rich groups (Figure 2).

Racial segregation and heat stress burden

The above analysis addresses income disparities but is silent on race. To examine racial inequalities, we divided the data for each census tract into white and non-white populations and calculated a dissimilarity index (*DI*) between the two groups. *DI* has been frequently used to examine residential segregation[57] and is a consolidated measure of the fraction of a population (say, for a census tract) that would need to change their residence to have the same distribution as the city it belongs to. It is given by:

$$DI = \frac{1}{2}\sum_{i=1}^{N}\left|\frac{w_i}{W} - \frac{nw_i}{NW}\right|, \qquad \text{(Equation 8)}$$

where i is one of the N census tracts within a city, w_i and nw_i are the white and non-white populations, respectively, in the ith census tract, and W and NW are the total white and non-white populations, respectively, for the city. The *DI* value from Equation 8 can range from 0 to 1, with 0 representing complete integration and 1 representing complete segregation. We used the mean segregation index of the 481 urban areas to divide them into lower than and high than average groups of residential segregation.

To calculate *HI* exposure inequities by race, we calculated another *CI* using Equation 7, but tracts were now ranked by proportion of white population, rather than income.[94,95] Finally, we calculated two other indices to examine segregation between white and non-white populations, one by calculating a Gini coefficient by replacing income with the proportion of white residents when calculating the Lorenz curve and another—Theil's entropy index—for white and non-white populations using the segregation package for the R programming language.[59] The results are shown in Figure S4.

SUPPLEMENTAL INFORMATION

Supplemental information can be found online at https://doi.org/10.1016/j.oneear.2023.05.016.

ACKNOWLEDGMENTS

Pacific Northwest National Laboratory is operated for the U.S. Department of Energy (DOE) by Battelle Memorial Institute under contract DE-AC05-76RL01830. This study is based on the work supported by Coastal Observations, Mechanisms, and Predictions Across Systems and Scales-Great Lakes Modeling (COMPASS-GLM) and Integrated Coastal Modeling (ICoM) projects, both of which are multi-institutional projects supported by DOE's Office of Science's Office of Biological and Environmental Research as part of the Earth and Environmental Systems Modeling program. T.C. and Y.Q. were supported by the Regional and Global Modeling and Analysis program area of COMPASS-GLM and ICoM. A.J.N. was funded by the NIH National Institute of Environmental Health Sciences (R01ES028346) and supported by the National Center for Atmospheric Research, which is a major facility sponsored by the National Science Foundation under Cooperative Agreement No. 1852977.

AUTHOR CONTRIBUTIONS

T.C. designed the study, performed the analysis, and wrote the first draft of the manuscript. A.J.N. performed the HRLDAS model simulations and the bias correction of simulated air temperature. A.J.N., Y.Q., A.H., and G.S. provided comments and suggestions on the research design and writing.

DECLARATION OF INTERESTS

The authors declare that they have no competing interests.

Received: September 14, 2022
Revised: March 3, 2023
Accepted: May 22, 2023
Published: June 16, 2023

REFERENCES

1. Elmqvist, T., Andersson, E., McPhearson, T., Bai, X., Bettencourt, L., Brondizio, E., Colding, J., Daily, G., Folke, C., Grimm, N., et al. (2021). Urbanization in and for the anthropocene. npj Urban Sustain. *1*, 6. https://doi.org/10.1038/s42949-021-00018-w.
2. Turner, W.R., Nakamura, T., and Dinetti, M. (2004). Global urbanization and the separation of humans from nature. Bioscience *54*, 585–590.
3. Qian, Y., Chakraborty, T.C., Li, J., Li, D., He, C., Sarangi, C., Chen, F., Yang, X., and Leung, L.R. (2022). Urbanization impact on regional climate and extreme weather: current understanding, uncertainties, and future research directions. Adv. Atmos. Sci. *39*, 819–860. https://doi.org/10.1007/s00376-021-1371-9.
4. United Nations (2018). Revision of World Urbanization Prospects (U. N. N. Y.).
5. Bertinelli, L., and Zou, B. (2008). Does urbanization foster human capital accumulation? J. Dev. Areas *41*, 171–184.
6. Pandey, B., Brelsford, C., and Seto, K.C. (2022). Infrastructure inequality is a characteristic of urbanization. Proc. Natl. Acad. Sci. USA *119*, e2119890119.
7. Nardone, A., Chiang, J., and Corburn, J. (2020). Historic redlining and urban health today in US cities. Environ. Justice *13*, 109–119.
8. Kramer, A. (2018). The unaffordable city: housing and transit in North American cities. Cities *83*, 1–10.
9. Glaeser, E.L., Kahn, M.E., and Rappaport, J. (2008). Why do the poor live in cities? The role of public transportation. J. Urban Econ. *63*, 1–24.
10. Stokes, E.C., and Seto, K.C. (2018). Tradeoffs in environmental and equity gains from job accessibility. Proc. Natl. Acad. Sci. USA *115*, E9773–E9781.
11. Nardone, A., Casey, J.A., Morello-Frosch, R., Mujahid, M., Balmes, J.R., and Thakur, N. (2020). Associations between historical residential redlining and current age-adjusted rates of emergency department visits due to asthma across eight cities in California: an ecological study. Lancet Planet. Health *4*, e24–e31.
12. Wilson, B. (2020). Urban heat management and the legacy of redlining. J. Am. Plann. Assoc. *86*, 443–457.
13. Hoffman, J.S., Shandas, V., and Pendleton, N. (2020). The effects of historical housing policies on resident exposure to intra-urban heat: a study of 108 us urban areas. Climate *8*, 12. https://doi.org/10.3390/cli8010012.
14. Krayenhoff, E.S., Moustaoui, M., Broadbent, A.M., Gupta, V., and Georgescu, M. (2018). Diurnal interaction between urban expansion, climate change and adaptation in US cities. Nat. Clim. Chang. *8*, 1097–1103. https://doi.org/10.1038/s41558-018-0320-9.
15. Tuholske, C., Caylor, K., Funk, C., Verdin, A., Sweeney, S., Grace, K., Peterson, P., and Evans, T. (2021). Global urban population exposure to extreme heat. Proc. Natl. Acad. Sci. USA *118*, e2024792118.
16. Heaviside, C., Macintyre, H., and Vardoulakis, S. (2017). The urban heat island: implications for health in a changing environment. Curr. Environ. Health Rep. *4*, 296–305.
17. Anderson, G.B., and Bell, M.L. (2011). Heat waves in the United States: mortality risk during heat waves and effect modification by heat wave characteristics in 43 US communities. Environ. Health Perspect. *119*, 210–218.
18. Zander, K.K., Botzen, W.J.W., Oppermann, E., Kjellstrom, T., and Garnett, S.T. (2015). Heat stress causes substantial labour productivity loss in Australia. Nat. Clim. Chang. *5*, 647–651. https://doi.org/10.1038/nclimate2623.

19. Perkins-Kirkpatrick, S.E., and Lewis, S.C. (2020). Increasing trends in regional heatwaves. Nat. Commun. *11*, 3357. https://doi.org/10.1038/s41467-020-16970-7.

20. Keith, L., Meerow, S., Hondula, D.M., Turner, V.K., and Arnott, J.C. (2021). Deploy heat officers, policies and metrics. Nature *598*, 29–31. https://doi.org/10.1038/d41586-021-02677-2.

21. Harlan, S.L., Brazel, A.J., Jenerette, G.D., Jones, N.S., Larsen, L., Prashad, L., and Stefanov, W.L. (2007). In the shade of affluence: the inequitable distribution of the urban heat island. In Equity and the Environment (Emerald Group Publishing Limited).

22. Voelkel, J., Hellman, D., Sakuma, R., and Shandas, V. (2018). Assessing vulnerability to urban heat: a study of disproportionate heat exposure and access to refuge by socio-demographic status in Portland, Oregon. Int. J. Environ. Res. Public Health *15*, 640.

23. Chakraborty, T., Hsu, A., Manya, D., and Sheriff, G. (2019). Disproportionately higher exposure to urban heat in lower-income neighborhoods: a multi-city perspective. Environ. Res. Lett. *14*, 105003. https://doi.org/10.1088/1748-9326/ab3b99.

24. Hsu, A., Sheriff, G., Chakraborty, T., and Manya, D. (2021). Disproportionate exposure to urban heat island intensity across major US cities. Nat. Commun. *12*, 2721. https://doi.org/10.1038/s41467-021-22799-5.

25. Muller, C.L., Chapman, L., Grimmond, C.S.B., Young, D.T., and Cai, X. (2013). Sensors and the city: a review of urban meteorological networks: sensors and the city. Int. J. Climatol. *33*, 1585–1600. https://doi.org/10.1002/joc.3678.

26. Ioannou, L.G., Mantzios, K., Tsoutsoubi, L., Notley, S.R., Dinas, P.C., Brearley, M., Epstein, Y., Havenith, G., Sawka, M.N., Bröde, P., et al. (2022). Indicators to assess physiological heat strain – Part 1: systematic review. Temperature *9*, 227–262. https://doi.org/10.1080/23328940.2022.2037376.

27. Harlan, S.L., Brazel, A.J., Prashad, L., Stefanov, W.L., and Larsen, L. (2006). Neighborhood microclimates and vulnerability to heat stress. Soc. Sci. Med. *63*, 2847–2863.

28. Ho, H.C., Knudby, A., Xu, Y., Hodul, M., and Aminipouri, M. (2016). A comparison of urban heat islands mapped using skin temperature, air temperature, and apparent temperature (Humidex), for the greater Vancouver area. Sci. Total Environ. *544*, 929–938. https://doi.org/10.1016/j.scitotenv.2015.12.021.

29. Kelly Turner, V., Rogers, M.L., Zhang, Y., Middel, A., Schneider, F.A., Ocón, J.P., Seeley, M., and Dialesandro, J. (2022). More than surface temperature: mitigating thermal exposure in hyper-local land system. J. Land Use Sci. *17*, 79–99. https://doi.org/10.1080/1747423X.2021.2015003.

30. Benz, S.A., Davis, S.J., and Burney, J.A. (2021). Drivers and projections of global surface temperature anomalies at the local scale. Environ. Res. Lett. *16*, 064093. https://doi.org/10.1088/1748-9326/ac0661.

31. Mentaschi, L., Duveiller, G., Zulian, G., Corbane, C., Pesaresi, M., Maes, J., Stocchino, A., and Feyen, L. (2022). Global long-term mapping of surface temperature shows intensified intra-city urban heat island extremes. Glob. Environ. Change *72*, 102441.

32. Sarangi, C., Qian, Y., Li, J., Leung, L.R., Chakraborty, T.C., and Liu, Y. (2021). Urbanization amplifies nighttime heat stress on warmer days over the US. Geophys. Res. Lett. *48*, e2021GL095678.

33. Huang, K., Lee, X., Stone, B., Jr., Knievel, J., Bell, M.L., and Seto, K.C. (2021). Persistent increases in nighttime heat stress from urban expansion despite heat island mitigation. JGR. Atmospheres *126*, e2020JD033831.

34. Zhou, B., Kaplan, S., Peeters, A., Kloog, I., and Erell, E. (2020). Surface,"“satellite” or “simulation”: mapping intra-urban microclimate variability in a desert city. Int. J. Climatol. *40*, 3099–3117.

35. Venter, Z.S., Chakraborty, T., and Lee, X. (2021). Crowdsourced air temperatures contrast satellite measures of the urban heat island and its mechanisms. Sci. Adv. *7*, eabb9569. https://doi.org/10.1126/sciadv.abb9569.

36. Chakraborty, T., Venter, Z.S., Qian, Y., and Lee, X. (2022). Lower urban humidity moderates outdoor heat stress. AGU Adv *3*, e2022AV000729.

37. Vargo, J., Stone, B., Habeeb, D., Liu, P., and Russell, A. (2016). The social and spatial distribution of temperature-related health impacts from urban heat island reduction policies. Environ. Sci. Policy *66*, 366–374.

38. Zhao, L., Oleson, K., Bou-Zeid, E., Krayenhoff, E.S., Bray, A., Zhu, Q., Zheng, Z., Chen, C., and Oppenheimer, M. (2021). Global multi-model projections of local urban climates. Nat. Clim. Chang. *11*, 152–157.

39. Schwaab, J., Meier, R., Mussetti, G., Seneviratne, S., Bürgi, C., and Davin, E.L. (2021). The role of urban trees in reducing land surface temperatures in European cities. Nat. Commun. *12*, 6763.

40. Ziter, C.D., Pedersen, E.J., Kucharik, C.J., and Turner, M.G. (2019). Scale-dependent interactions between tree canopy cover and impervious surfaces reduce daytime urban heat during summer. Proc. Natl. Acad. Sci. USA *116*, 7575–7580. https://doi.org/10.1073/pnas.1817561116.

41. Krupka, D.J. (2007). Are big cities more segregated? Neighbourhood scale and the measurement of segregation. Urban Stud. *44*, 187–197.

42. Depersin, J., and Barthelemy, M. (2018). From global scaling to the dynamics of individual cities. Proc. Natl. Acad. Sci. USA *115*, 2317–2322.

43. Xu, Y., Olmos, L.E., Abbar, S., and González, M.C. (2020). Deconstructing laws of accessibility and facility distribution in cities. Sci. Adv. *6*, eabb4112. https://doi.org/10.1126/sciadv.abb4112.

44. Frey, W.H. (1979). Central city white flight: racial and nonracial causes. Am. Sociol. Rev. *44*, 425. https://doi.org/10.2307/2094885.

45. An, B., Orlando, A.W., and Rodnyansky, S. (2019). The physical legacy of racism: how redlining cemented the modern built environment. SSRN J. https://doi.org/10.2139/ssrn.3500612.

46. Shertzer, A., and Walsh, R.P. (2019). Racial sorting and the emergence of segregation in American cities. Rev. Econ. Stat. *101*, 415–427.

47. Juday, L.J. (2015). The changing shape of American cities. *Demographics Research Group Weldon Cooper* (Center for Public Service: University of Virginia).

48. Nelson, R.K., Winling, L., Marciano, R., Connolly, N., and Ayers, E.L. (2020). Mapping inequality: redlining in new deal America. Am. Panor. Atlas U. S. Hist. Univ. Richmond Digit. Scholarsh. Lab *17*, 19.

49. Chakraborty, T., Hsu, A., Manya, D., and Sheriff, G. (2020). A spatially explicit surface urban heat island database for the United States: characterization, uncertainties, and possible applications. ISPRS J. Photogramm. Remote Sens. *168*, 74–88.

50. Benz, S.A., and Burney, J.A. (2021). Widespread race and class disparities in surface urban heat extremes across the United States. Earth's Future *9*. e2021EF002016. https://doi.org/10.1029/2021EF002016.

51. McDonald, R.I., Biswas, T., Sachar, C., Housman, I., Boucher, T.M., Balk, D., Nowak, D., Spotswood, E., Stanley, C.K., and Leyk, S. (2021). The tree cover and temperature disparity in US urbanized areas: quantifying the association with income across 5,723 communities. PLoS One *16*, e0249715.

52. Wu, S., Yu, W., and Chen, B. (2023). Observed inequality in thermal comfort exposure and its multifaceted associations with greenspace in United States cities. Landsc. Urban Plan. *233*, 104701.

53. Chakraborty, T., Hsu, A., Manya, D., and Sheriff, G. (2020). A spatially explicit surface urban heat island database for the United States: characterization, uncertainties, and possible applications. ISPRS J. Photogramm. Remote Sens. *168*, 74–88. https://doi.org/10.1016/j.isprsjprs.2020.07.021.

54. Semenza, J.C., Rubin, C.H., Falter, K.H., Selanikio, J.D., Flanders, W.D., Howe, H.L., and Wilhelm, J.L. (1996). Heat-related deaths during the july 1995 heat wave in Chicago. N. Engl. J. Med. *335*, 84–90. https://doi.org/10.1056/NEJM199607113350203.

55. Wang, J., Qian, Y., Pringle, W., Chakraborty, T.C., Hetland, R., Yang, Z., and Xue, P. (2023). Contrasting effects of lake breeze and urbanization on heat stress in Chicago metropolitan area. Urban Clim. *48*, 101429. https://doi.org/10.1016/j.uclim.2023.101429.

56. Woo, B., Kravitz-Wirtz, N., Sass, V., Crowder, K., Teixeira, S., and Takeuchi, D.T. (2019). Residential segregation and racial/ethnic disparities in ambient air pollution. Race Soc. Probl. *11*, 60–67.

57. Massey, D.S., and Denton, N.A. (1988). The dimensions of residential segregation. Soc. Forces *67*, 281–315.

58. James, D.R., and Taeuber, K.E. (1985). Measures of segregation. Sociol. Methodol. *15*, 1–32.

59. Elbers, B. (2023). A method for studying differences in segregation across time and space. Sociol. Methods Res. *52*, 5–42.

60. Theil, H. (1971). Principles of Econometrics.

61. Nesbitt, L., Meitner, M.J., Girling, C., Sheppard, S.R., and Lu, Y. (2019). Who has access to urban vegetation? A spatial analysis of distributional green equity in 10 US cities. Landsc. Urban Plan. *181*, 51–79.

62. Rothwell, J.T., and Massey, D.S. (2010). Density zoning and class segregation in US metropolitan areas. Soc. Sci. Q. *91*, 1123–1143.

63. Locke, D.H., Hall, B., Grove, J.M., Pickett, S.T.A., Ogden, L.A., Aoki, C., Boone, C.G., and O'Neil-Dunne, J.P.M. (2021). Residential housing segregation and urban tree canopy in 37 US Cities. npj Urban Sustain. *1*, 15.

64. Burghardt, K.T., Avolio, M.L., Locke, D.H., Grove, J.M., Sonti, N.F., and Swan, C.M. (2023). Current Street Tree Communities Reflect Race-based Housing Policy and Modern Attempts to Remedy Environmental Injustice (Wiley Online Library).

65. Zhang, T., Zhou, Y., Zhao, K., Zhu, Z., Chen, G., Hu, J., and Wang, L. (2022). A global dataset of daily maximum and minimum near-surface air temperature at 1 km resolution over land (2003–2020). Earth Syst. Sci. Data *14*, 5637–5649.

66. Sherwood, S.C. (2018). How important is humidity in heat stress? J. Geophys. Res. Atmos. *123*, 11808–11810. https://doi.org/10.1029/2018JD028969.

67. Middel, A., Alkhaled, S., Schneider, F.A., Hagen, B., and Coseo, P. (2021). 50 Grades of shade. Bull. Am. Meteorol. Soc. 1–35. https://doi.org/10.1175/BAMS-D-20-0193.1.

68. Chakraborty, T., Biswas, T., Campbell, L.S., Franklin, B., Parker, S.S., and Tukman, M. (2022). Feasibility of afforestation as an equitable nature-based solution in urban areas. Sustain. Cities Soc. *81*, 103826.

69. Gould, K., and Lewis, T. (2016). Green Gentrification 0, ed. (Routledge). https://doi.org/10.4324/9781315687322.

70. Klaiber, H.A., Abbott, J.K., and Smith, V.K. (2017). Some like it (less) hot: extracting trade-off measures for physically coupled amenities. J. Assoc. Environ. Resour. Econ. *4*, 1053–1079. https://doi.org/10.1086/692842.

71. Zhao, L., Lee, X., and Schultz, N.M. (2017). A wedge strategy for mitigation of urban warming in future climate scenarios. Atmos. Chem. Phys. *17*, 9067–9080. https://doi.org/10.5194/acp-17-9067-2017.

72. Sproul, J., Wan, M.P., Mandel, B.H., and Rosenfeld, A.H. (2014). Economic comparison of white, green, and black flat roofs in the United States. Energy Build. *71*, 20–27. https://doi.org/10.1016/j.enbuild.2013.11.058.

73. Fishman, R., Carrillo, P., and Russ, J. (2019). Long-term impacts of exposure to high temperatures on human capital and economic productivity. J. Environ. Econ. Manage. *93*, 221–238.

74. 2010 census urban and rural classification and urban area criteria https://www.census.gov/programs-surveys/geography/guidance/geo-areas/urban-rural/2010-urban-rural.html.

75. Mather, M., Rivers, K.L., and Jacobsen, L.A. (2005). The American Community Survey (Population Reference Bureau).

76. Chen, F., Manning, K.W., LeMone, M.A., Trier, S.B., Alfieri, J.G., Roberts, R., Tewari, M., Niyogi, D., Horst, T.W., Oncley, S.P., et al. (2007). Description and evaluation of the characteristics of the NCAR high-resolution land data assimilation system. J. Appl. Meteorol. Climatol. *46*, 694–713.

77. Xia, Y., Mitchell, K., Ek, M., Sheffield, J., Cosgrove, B., Wood, E., Luo, L., Alonge, C., Wei, H., Meng, J., et al. (2012). Continental-scale water and energy flux analysis and validation for the North American Land Data Assimilation System project phase 2 (NLDAS-2): 1. Intercomparison and application of model products. J. Geophys. Res. *117*.

78. Skamarock, W.C., Klemp, J.B., Dudhia, J., Gill, D.O., Barker, D.M., Wang, W., and Powers, J.G. (2008). A Description of the Advanced Research WRF Version 3. NCAR Technical note-475+ STR.

79. Monaghan, A.J., Hu, L., Brunsell, N.A., Barlage, M., and Wilhelmi, O.V. (2014). Evaluating the impact of urban morphology configurations on the accuracy of urban canopy model temperature simulations with MODIS. J. Geophys. Res. Atmos. *119*, 6376–6392.

80. Niu, G.-Y., Yang, Z.-L., Mitchell, K.E., Chen, F., Ek, M.B., Barlage, M., Kumar, A., Manning, K., Niyogi, D., Rosero, E., et al. (2011). The community Noah land surface model with multiparameterization options (Noah-MP): 1. Model description and evaluation with local-scale measurements. J. Geophys. Res. *116*, D12109.

81. Kusaka, H., Kondo, H., Kikegawa, Y., and Kimura, F. (2001). A simple single-layer urban canopy model for atmospheric models: comparison with multi-layer and slab models. Bound. Layer Meteorol. *101*, 329–358.

82. Wickham, J., Stehman, S.V., Sorenson, D.G., Gass, L., and Dewitz, J.A. (2021). Thematic accuracy assessment of the NLCD 2016 land cover for the conterminous United States. Remote Sens. Environ. *257*, 112357.

83. Thornton, M.M., Shrestha, R., Wei, Y., Thornton, P.E., Kao, S., and Wilson, B.E. (2020). DaymetDaymet: Daily Surface Weather Data on a 1-km Grid for North America. Version 4. 0 MB. 10.3334/ORNLDAAC/1840.

84. Thomas, N., Ebelt, S.T., Newman, A.J., Scovronick, N., D'Souza, R.R., Moss, S.E., Warren, J.L., Strickland, M.J., Darrow, L.A., and Chang, H.H. (2021). Time-series analysis of daily ambient temperature and emergency department visits in five US cities with a comparison of exposure metrics derived from 1-km meteorology products. Environ. Health. *20*, 55.

85. Menne, M.J., Durre, I., Vose, R.S., Gleason, B.E., and Houston, T.G. (2012). An overview of the global historical climatology network-daily database. J. Atmos. Ocean. Technol. *29*, 897–910.

86. Rothfusz, L.P. (1990). The heat index equation. In (or, more than you ever wanted to know about heat index), *9023* (Fort Worth, Texas: National Oceanic and Atmospheric Administration, National Weather Service, Office of Meteorology), p. 640.

87. Wan, Z. (2014). New refinements and validation of the collection-6 MODIS land-surface temperature/emissivity product. Remote Sens. Environ. *140*, 36–45.

88. Roy, D.P., Wulder, M.A., Loveland, T.R., Ce, W., Allen, R.G., Anderson, M.C., Helder, D., Irons, J.R., Johnson, D.M., Kennedy, R., et al. (2014). Landsat-8: science and product vision for terrestrial global change research. Remote Sens. Environ. *145*, 154–172.

89. Ermida, S.L., Soares, P., Mantas, V., Göttsche, F.M., and Trigo, I.F. (2020). Google earth engine open-source code for land surface temperature estimation from the landsat series. Remote Sens. *12*, 1471.

90. Chakraborty, T.C., Lee, X., Ermida, S., and Zhan, W. (2021). On the land emissivity assumption and Landsat-derived surface urban heat islands: a global analysis. Remote Sens. Environ. *265*, 112682.

91. Maguire, K., and Sheriff, G. (2011). Comparing distributions of environmental outcomes for regulatory environmental justice analysis. Int. J. Environ. Res. Public Health *8*, 1707–1726. https://doi.org/10.3390/ijerph8051707.

92. Lorenz, M.O. (1905). Methods of measuring the concentration of wealth. Publ. Am. Stat. Assoc. *9*, 209–219. https://doi.org/10.1080/15225437.1905.10503443.

93. Wagstaff, A., Paci, P., and van Doorslaer, E. (1991). On the measurement of inequalities in health. Soc. Sci. Med. *33*, 545–557. https://doi.org/10.1016/0277-9536(91)90212-U.

94. Su, J.G., Morello-Frosch, R., Jesdale, B.M., Kyle, A.D., Shamasunder, B., and Jerrett, M. (2009). An Index for Assessing Demographic Inequalities in Cumulative Environmental Hazards with Application to Los Angeles, California (ACS Publications).

95. Cushing, L., Faust, J., August, L.M., Cendak, R., Wieland, W., and Alexeeff, G. (2015). Racial/ethnic disparities in cumulative environmental health impacts in California: evidence from a statewide environmental justice screening tool (CalEnviroScreen 1.1). Am. J. Public Health *105*, 2341–2348.

One Earth, Volume *6*

Supplemental information

Residential segregation and outdoor urban moist heat stress disparities in the United States

TC Chakraborty, Andrew J. Newman, Yun Qian, Angel Hsu, and Glenn Sheriff

Note S1: Difference between satellite-derived land surface temperature and modeled skin temperature, and a discussion on uncertainties

The different sensitivities of MODIS-derived LST and modeled *Tsk* seen in the present study (Figures 2A and S3) require further clarification. The satellite-derived radiative skin temperature, often called LST, as seen from the view angle and at the resolution of MODIS imagery, largely comprises of thermal emission from rooftops and taller vertical facades, but rarely road temperatures[1,2]. An example of this satellite view's influence on LST estimates can be seen when comparing LST anomalies across HOLC grades from MODIS and Landsat (Figure S6). Landsat 8 has a finer resolution (≈100 m) compared to MODIS (≈1000 m) and a narrower field of view, making it capable of picking up more thermal emissions from roads than MODIS[3]. Overall, the LST anomalies are stronger for Landsat (-1.49 ˚C for grade A to 0.69 ˚C for grade D) compared to that for MODIS (-0.78 C to 0.4 C). These differences are in line with consistently higher magnitudes of surface urban heat island seen when using Landsat data instead of MODIS[4]. In contrast, *Tsk* represents a more complete radiative skin temperature and the integral of the skin temperature from the walls, roads, and roofs of the urban canopy represented in the model[5]. Moreover, these satellites cannot capture the thermal environment under shade (from buildings or trees) or for cloudy conditions[6]. On the other hand, the model provides all-sky estimates that considers the complete urban fabric.

It is important to note that radiant heat exposure is only one part of the overall physiological response to heat, and does not tell as much about *Ta* and RH within urban areas, which are critical for quantifying moist heat stress[7,8]. However, the relative importance of humidity for heat stress (compared to *Ta*) remains an open question[9,10]. We use two operational metrics of heat stress, with HI being more temperature-sensitive than Humidex[10]. Using Humidex, which is more dependent on moisture content, shows a further reduction in the sensitivity of heat stress to socioeconomic variables compared to that in *Ta*. For instance, the median sensitivity per $10,000 rise in income is -1.33 for Humidex vs -1.36 ˚C for *Ta*. Noting the different valid range of values for *Ta* and Humidex, the sensitivity of Humidex to income further reduces versus that of *Ta* when both variables are standardized (forced to vary between 0 and 1). The standardized Humidex reduces by -0.015 for every $10,000 greater income versus a reduction of -0.018 for standardized *Ta* (Figure S10A). Similar results are seen for standardized sensitivities by race (Figure S10). Since the model simulations only include maximum and minimum q2, we calculate the lower bound for

maximum HI using maximum *Ta* and minimum q2 (since RH is generally lowest when *Ta* peaks during the diurnal cycle[11]). We also confirm that disparities in the upper bound (or maximum possible HI), calculated from maximum *Ta* and maximum q2, are also pervasive across these cities and less sensitive to socioeconomic variables than *Tsk* (Figure S11).

Finally, there are still large uncertainties in urban representations in models, especially at these scales[12]. Moreover, since the land-surface model used here was run in uncoupled mode to achieve high spatial resolution (≈1 km) and long temporal (daily summaries for 30+ years) extent, this would impact the magnitude of the *Tsk*, *Ta*, and heat stress disparities found in the present study. We minimize potential errors in *Ta* by bias correcting the simulated *Ta* using observation fields. Similar errors due to biases in RH is expected to be minimal since *Ta* is several times more important than RH for operational metrics of moist heat stress[13]. Moreover, the bias correction of *Ta* also impacts RH since the model simulates *q2*, and RH is also a strong function of *Ta*. More importantly, both observational and coupled modeling studies confirm urban disparities in moist heat stress, with disparities being overestimated when using satellite-derived or modeled skin temperature, albeit these are for individual cities[14,15].

REFERENCES

1. Zhou, B., Kaplan, S., Peeters, A., Kloog, I., and Erell, E. (2020). "Surface,""satellite" or "simulation": Mapping intra-urban microclimate variability in a desert city. Int. J. Climatol. *40*, 3099–3117.

2. Kelly Turner, V., Rogers, M.L., Zhang, Y., Middel, A., Schneider, F.A., Ocón, J.P., Seeley, M., and Dialesandro, J. (2022). More than surface temperature: mitigating thermal exposure in hyper-local land system. J. Land Use Sci. *17*, 79–99. 10.1080/1747423X.2021.2015003.

3. Schaaf, C.B., Gao, F., Strahler, A.H., Lucht, W., Li, X., Tsang, T., Strugnell, N.C., Zhang, X., Jin, Y., and Muller, J.-P. (2002). First operational BRDF, albedo nadir reflectance products from MODIS. Remote Sens. Environ. *83*, 135–148.

4. Chakraborty, T.C., Lee, X., Ermida, S., and Zhan, W. (2021). On the land emissivity assumption and Landsat-derived surface urban heat islands: A global analysis. Remote Sens. Environ. *265*, 112682.

5. Stewart, I.D., Krayenhoff, E.S., Voogt, J.A., Lachapelle, J.A., Allen, M.A., and Broadbent, A.M. (2021). Time Evolution of the Surface Urban Heat Island. Earths Future *9*. 10.1029/2021EF002178.

6. Middel, A., Alkhaled, S., Schneider, F.A., Hagen, B., and Coseo, P. (2021). 50 Grades of Shade. Bull. Am. Meteorol. Soc., 1–35. 10.1175/BAMS-D-20-0193.1.

7. Venter, Z.S., Chakraborty, T., and Lee, X. (2021). Crowdsourced air temperatures contrast satellite measures of the urban heat island and its mechanisms. Sci. Adv. *7*, eabb9569. 10.1126/sciadv.abb9569.

8. Ioannou, L.G., Mantzios, K., Tsoutsoubi, L., Notley, S.R., Dinas, P.C., Brearley, M., Epstein, Y., Havenith, G., Sawka, M.N., Bröde, P., et al. (2022). Indicators to assess physiological heat strain – Part 1: Systematic review. Temperature, 1–36. 10.1080/23328940.2022.2037376.

9. Anderson, G.B., Bell, M.L., and Peng, R.D. (2013). Methods to Calculate the Heat Index as an Exposure Metric in Environmental Health Research. Environ. Health Perspect. *121*, 1111–1119. 10.1289/ehp.1206273.

10. Sherwood, S.C. (2018). How Important Is Humidity in Heat Stress? J. Geophys. Res. Atmospheres *123*. 10.1029/2018JD028969.

11. Fischer, E.M., and Schär, C. (2010). Consistent geographical patterns of changes in high-impact European heatwaves. Nat. Geosci. *3*, 398–403.

12. Qian, Y., Chakraborty, T.C., Li, J., Li, D., He, C., Sarangi, C., Chen, F., Yang, X., and Leung, L.R. (2022). Urbanization Impact on Regional Climate and Extreme Weather: Current Understanding, Uncertainties, and Future Research Directions. Adv. Atmospheric Sci. *39*, 819–860. 10.1007/s00376-021-1371-9.

13. Chakraborty, T., Venter, Z.S., Qian, Y., and Lee, X. (2022). Lower urban humidity moderates outdoor heat stress. AGU Adv. *3*, e2022AV000729.

14. Chakraborty, T., Wang, J., Qian, Y., Pringle, W., Yang, Z., and Xue, P. (In Review). Urban versus lake impacts on heat stress and its disparities in a shoreline city. 10.21203/rs.3.rs-1818535/v1.

15. Wang, X., Hsu, A., and Chakraborty, T. (In Review). Citizen and Machine Learning-aided high-resolution mapping of urban heat exposure and stress. 10.31223/X52M1M.

16. Zhang, T., Zhou, Y., Zhao, K., Zhu, Z., Chen, G., Hu, J., and Wang, L. (2022). A global dataset of daily maximum and minimum near-surface air temperature at 1 km resolution over land (2003–2020). Earth Syst. Sci. Data *14*, 5637–5649.

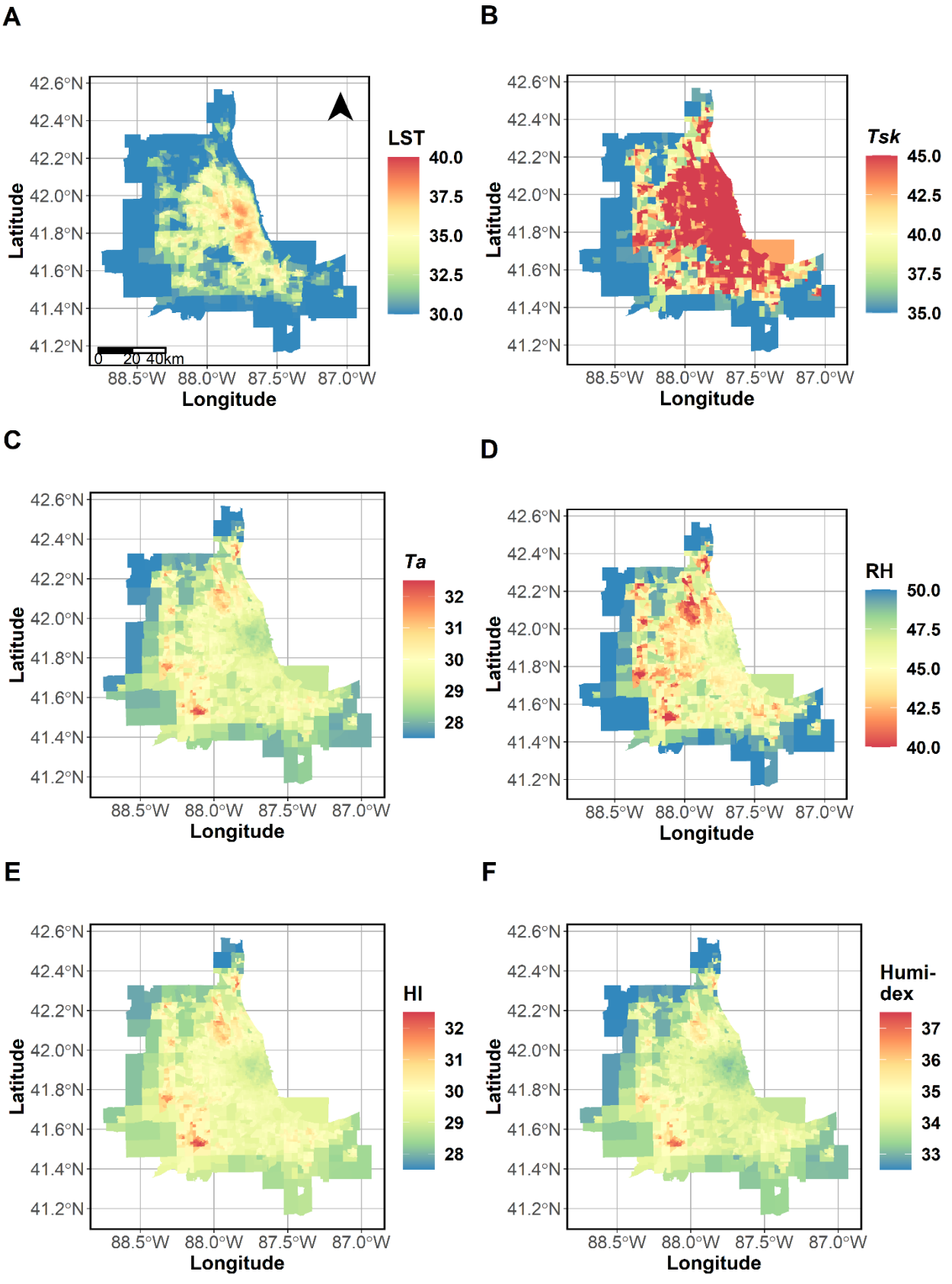
A
B
C
D
E
F
Latitude
Longitude
42.6°N
42.4°N
42.2°N
42.0°N
41.8°N
41.6°N
41.4°N
41.2°N
88.5°W
88.0°W
87.5°W
87.0°W
0 20 40km
LST
40.0
37.5
35.0
32.5
30.0
Tsk
45.0
42.5
40.0
37.5
35.0
Ta
32
31
30
29
28
RH
50.0
47.5
45.0
42.5
40.0
HI
32
31
30
29
28
Humi-
dex
37
36
35
34
33

Figure S1. Spatial variability over Chicago. Census-tract level variability in (A) satellite-derived daytime summer LST and average summer maximum of modeled (B) *Tsk*, (C) *Ta*, (D) RH, (E) HI, and (F) Humidex for the Chicago urbanized area. The same color bar range is used in all cases for easy comparison.

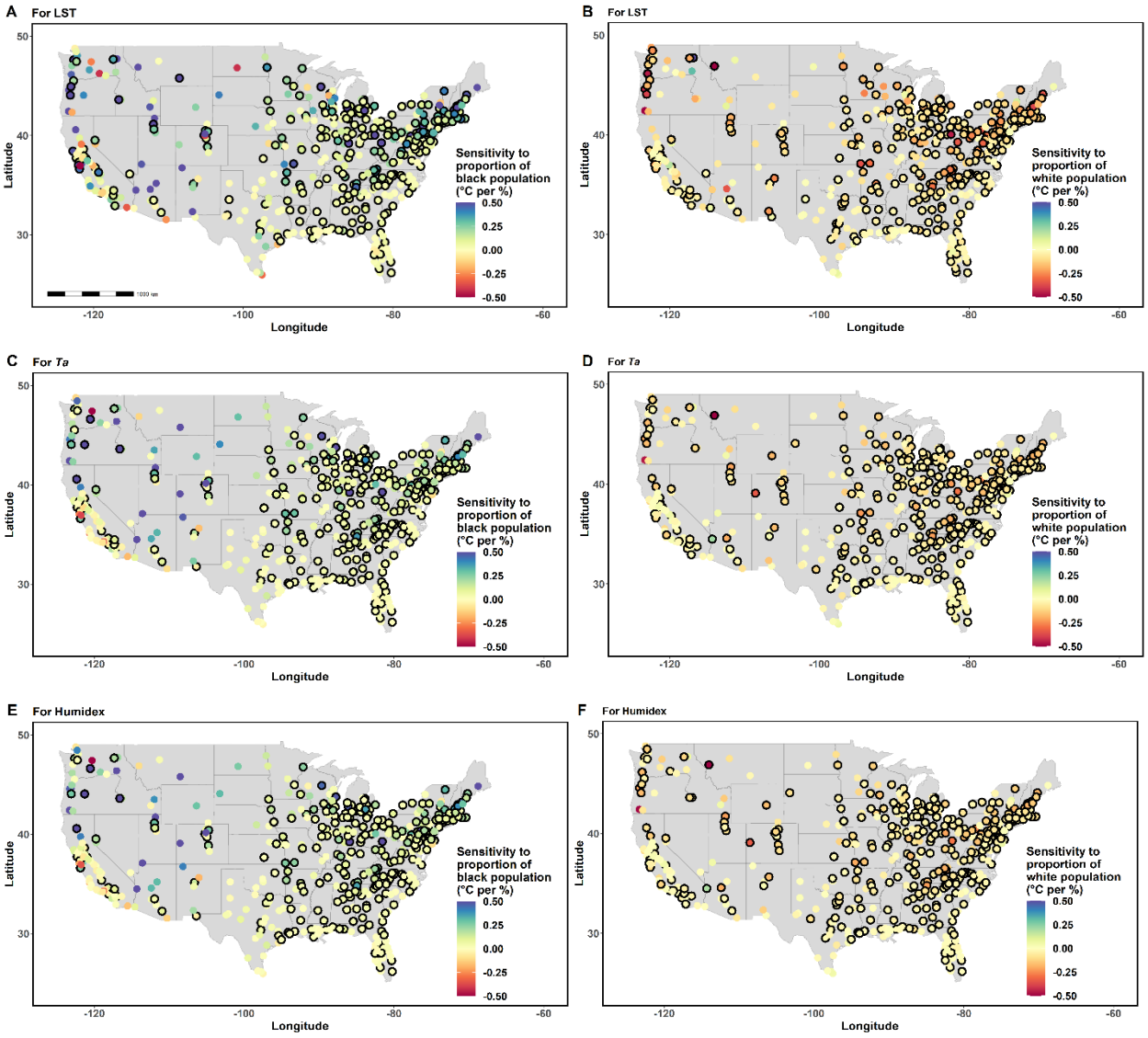

Figure S2. Disparities in heat exposure by race. (A), (C), and (E) show the slopes of the linear regressions between the proportion of black population in a census-tract and satellite-derived summer daytime LST, and the average summer maximum of *Ta* and Humidex, respectively for the 481 urbanized areas. (B), (D), and (F) are similar, but for the proportion of white population. Circles with black outlines represent statistically significant correlations ($p<0.01$).

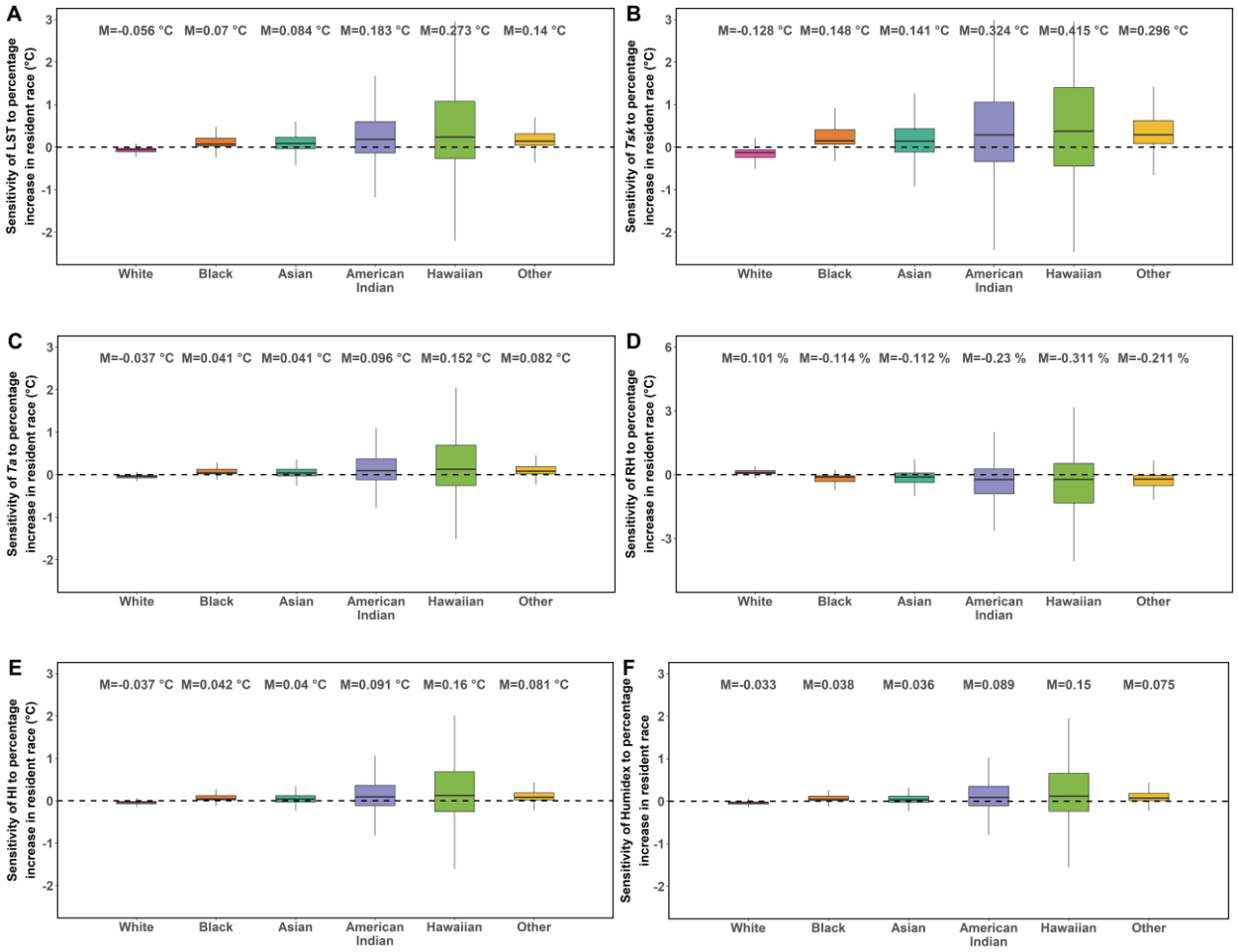

Figure S3. Disparities in heat exposure metrics for all races. Box and whisker plots summarizing the slopes of the linear regressions between the proportion of population of each race in a census-tract and (A) satellite-derived daytime summer LST and average summer maximum of modeled (B) *Tsk*, (C) *Ta*, (D) RH, (E) HI, and (F) Humidex for the 481 urbanized areas. The numbers at the top give median sensitivities of the variable to a percentage change in race of the population.

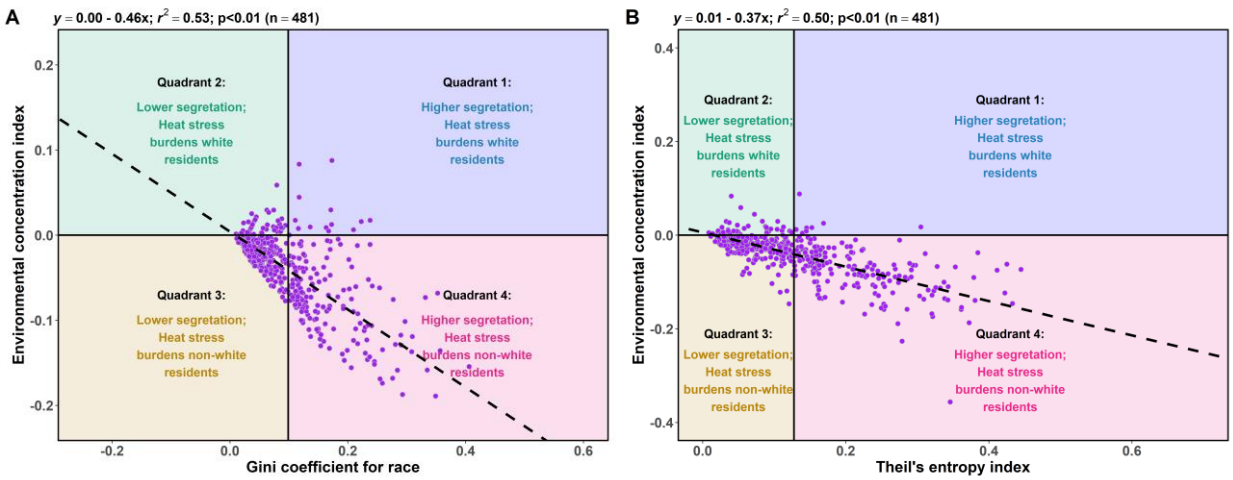

Figure S4. City typologies for residential segregation and heat stress inequalities using alternative metrics. (A) Four-quadrant plot of heat stress (HI) concentration index (based on proportion of white residents) and Gini coefficient (replacing income with proportion of white residents) for the 481 cities considered here. The quadrant threshold for residential segregation is the mean Gini coefficent for race of the sample (0.1) and the quadrant threshold for heat stress distributional inequity is 0. The line of best fit between city-level heat stress concentration index and Gini coefficient for race and the associated linear regression equation, coefficient of determination (r^2), p-value, and sample size (n) are noted. (B) is similar to (A) but uses Theil's entropy index instead of the Gini coefficient for race as the metric for segregation.

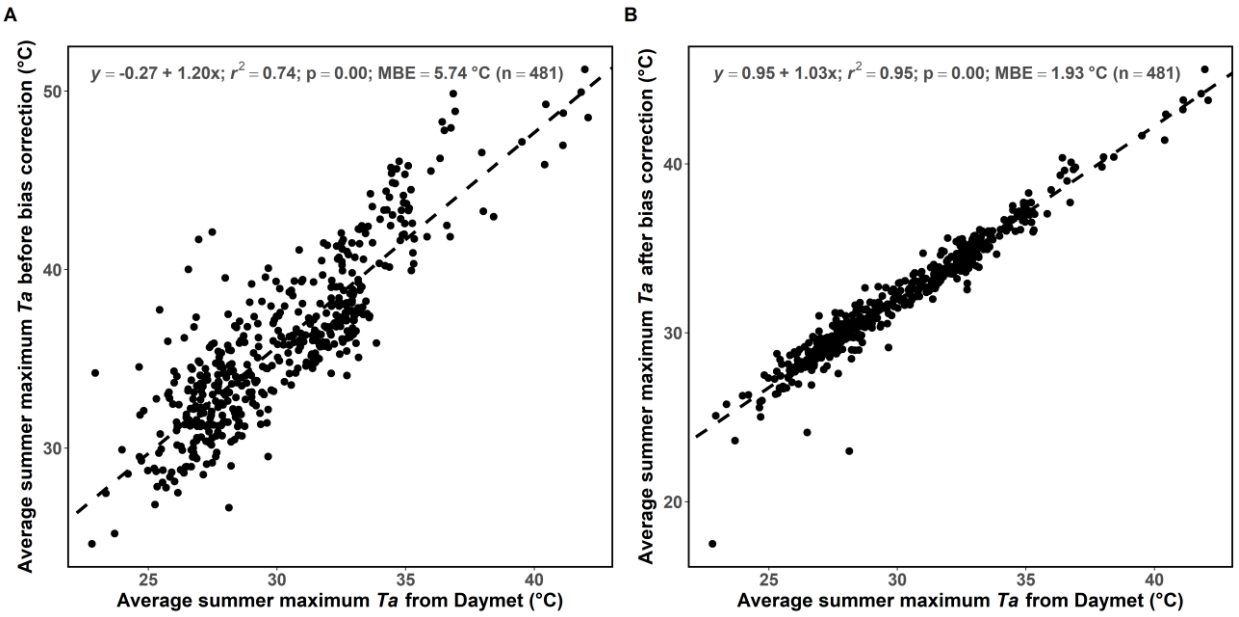

130

131 **Figure S5. Impact of bias correction on urban-scale average maximum summer air**
132 **temperature.** Correlations between the average summer maximum *Ta* from Daymet and the
133 corresponding simulated values in the present study (A) before and (B) after bias correction. The
134 mean bias error (MBE), coefficient of determination (r^2), p-value, and sample size (n) are noted.
135 Each sample corresponds to an urbanized area in the continental US.

136

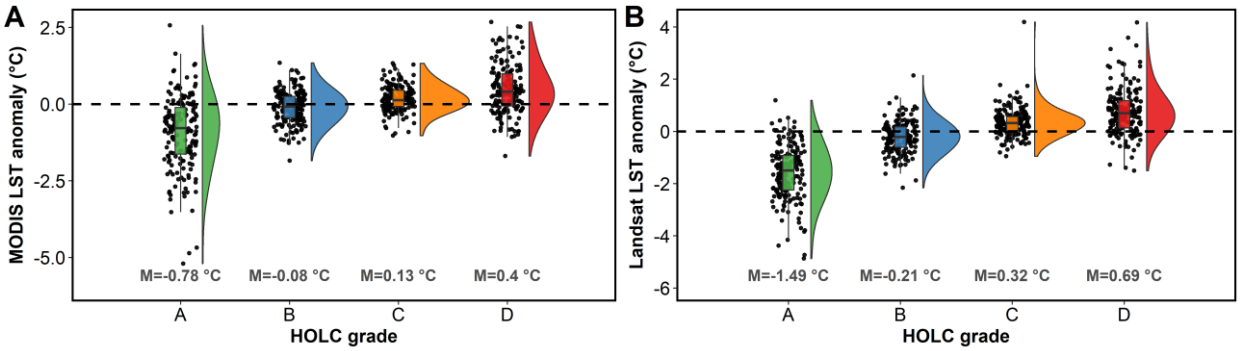

Figure S6. Land surface temperature anomalies by HOLC security rating for different satellites. The distributions of anomalies in (A) MODIS-derived and (B) Landsat-derived mean summer daytime LST across 171 cities. The numbers at the bottom give median anomalies for each group.

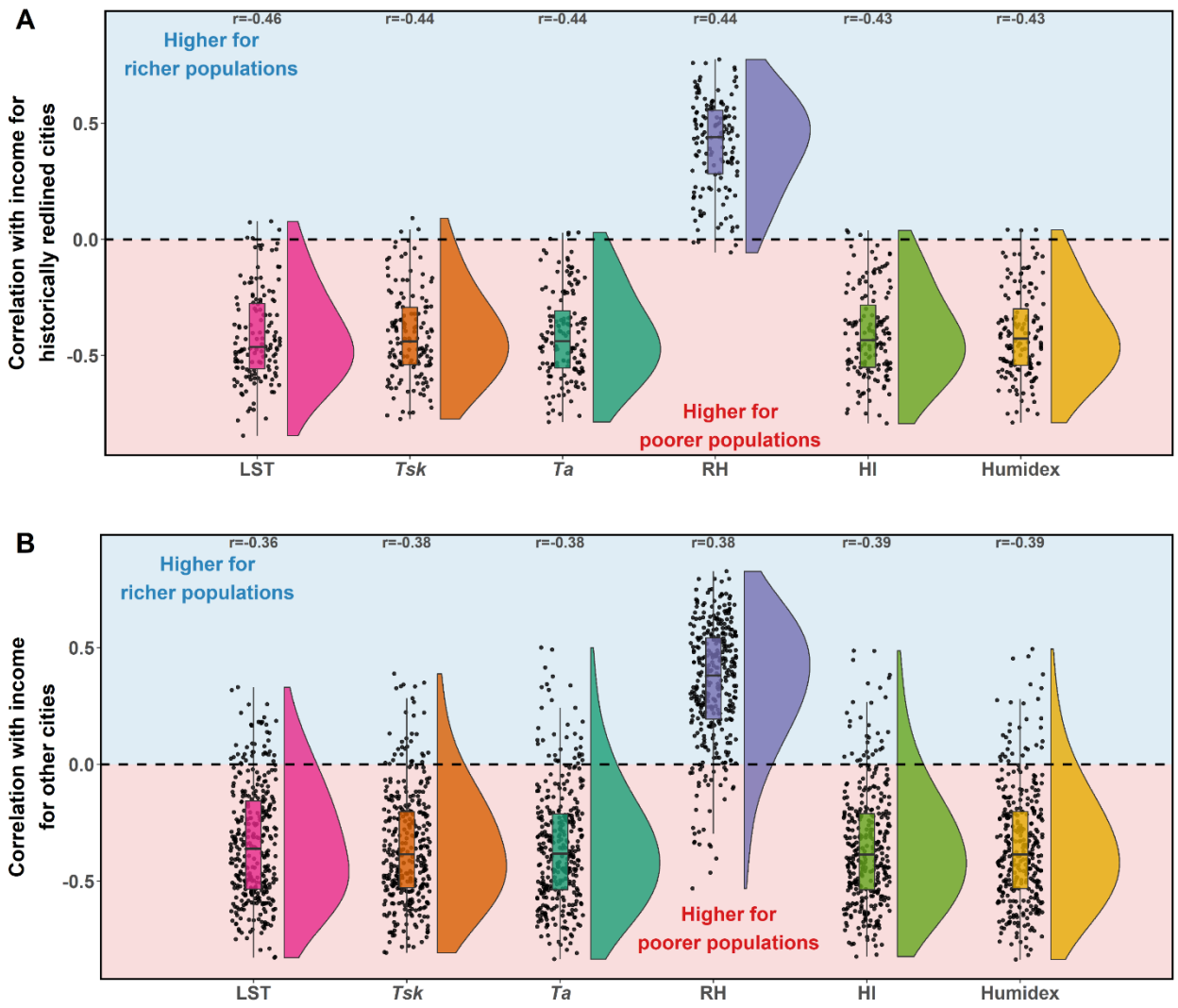

Figure S7. Correlations of heat exposure metrics with income for redlined versus other cities. (A) shows distributions of correlation coefficients of satellite-derived mean summer daytime LST and the average summer maximum of modeled *Tsk*, *Ta*, RH, HI, and Humidex with income across the 143 cities that overlap with any HOLC rated neighborhood (median correlation coefficient *r* for each variable is annotated). (B) is similar to (A), but for the 338 cities that do not overlap with any HOLC rated neighborhood.

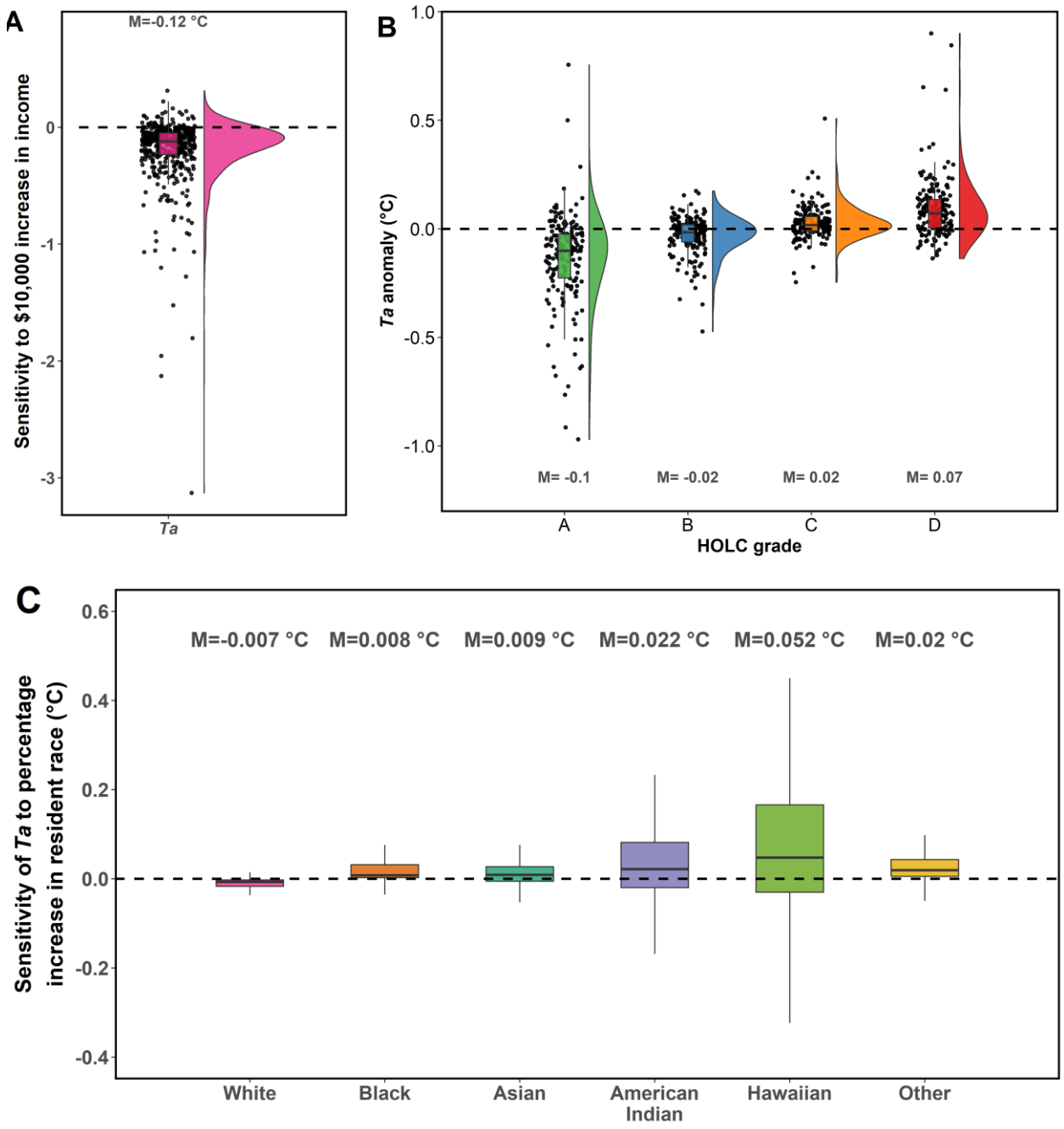

Figure S8. Distributions and disparities in air temperature based on gridded statistical dataset. Similar to Figures 3A, 5B, and S3C but based on a gridded 1 km near-surface *Ta* dataset using a statistical method constrained by MODIS-derived LST and ground observations[16].

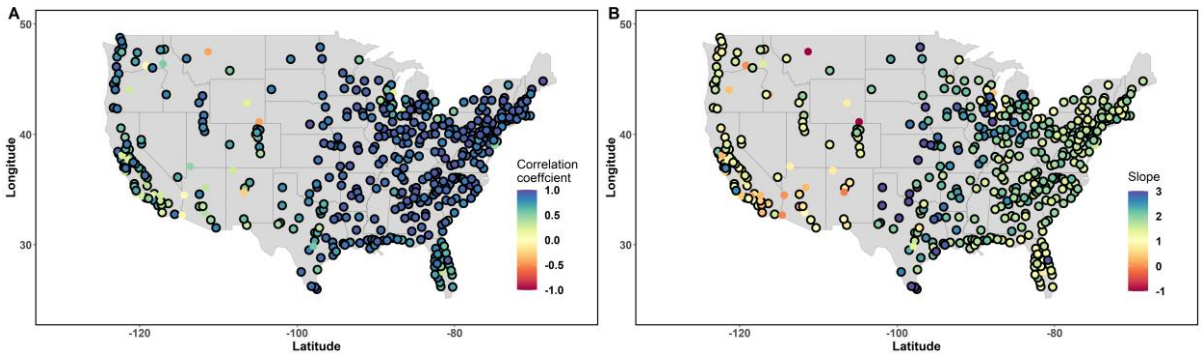

Figure S9. Model evaluation against satellite observations. (A) shows the correlation coefficient between census-tract level average summer maximum of modeled *Tsk* and satellite-derived summer daytime LST for the 481 urbanized areas. (B) is similar, but for the slope of the linear regressions between the two variables. Circles with black outlines represent statistically significant correlations ($p<0.01$).

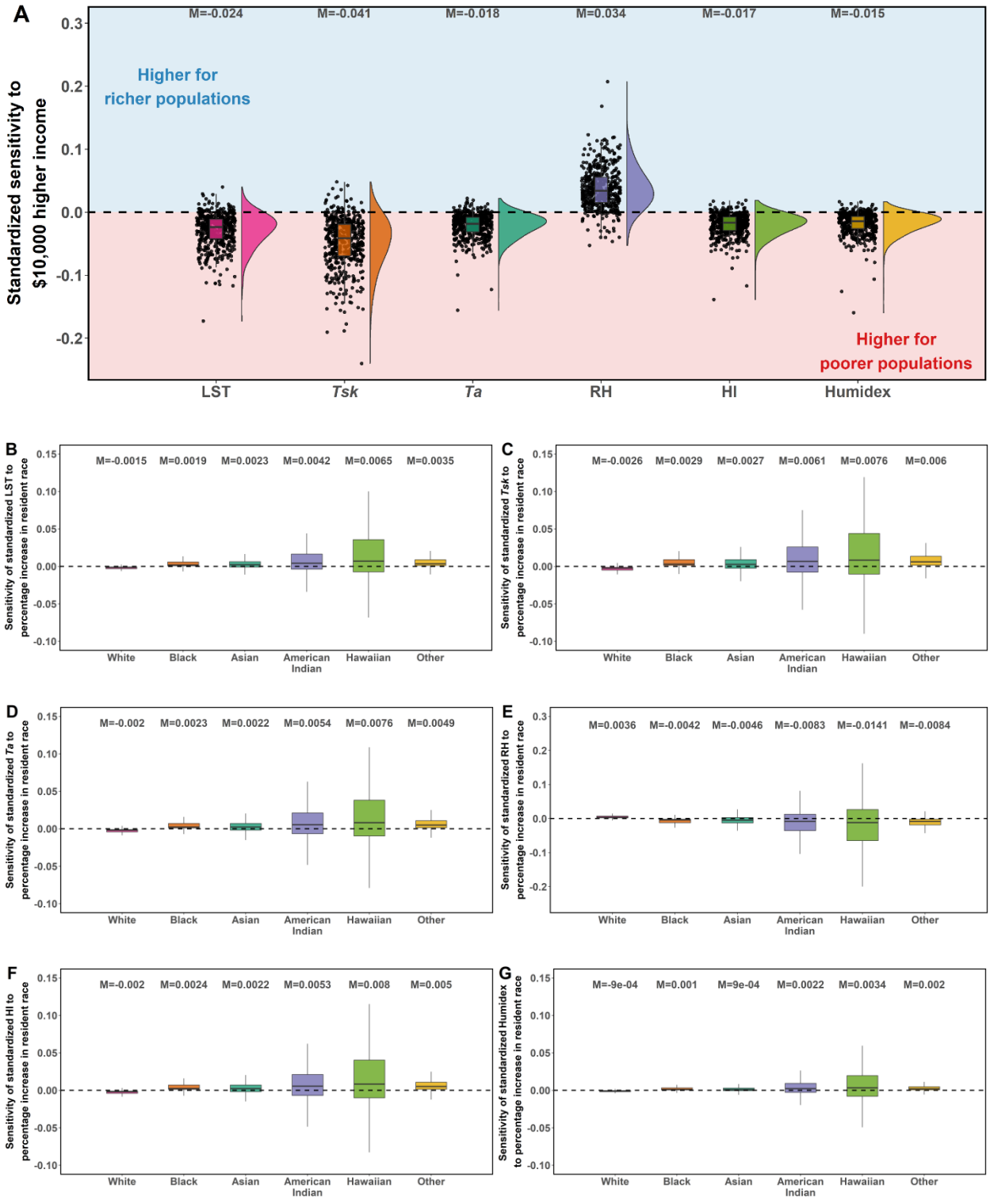

Figure S10. Standardized sensitivities to income and race. Similar to Figures 3A and S3A-S3G, but using standardized (range of 0 to 1) values of LST, *Tsk*, *Ta*, RH, HI, and Humidex as the

independent variables. The numbers at the top give the median standardized sensitivities of the variable to changes in income or percentage population of a particular race.

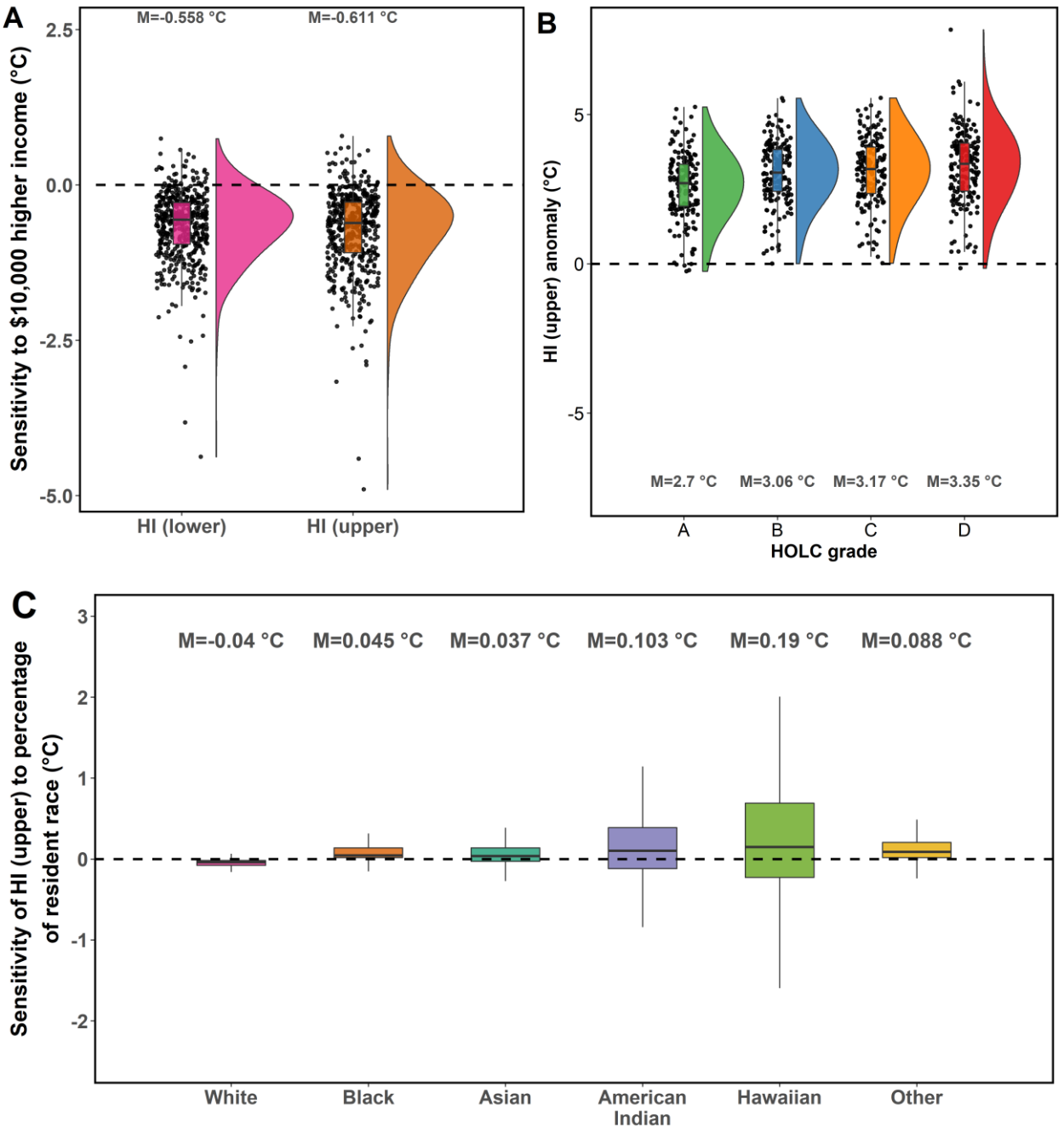

Figure S11. Examining upper and lower bounds of heat index. (A), (B), and (C) show the impacts of using average summer maximum specific humidity and 2-m air temperature to calculate heat index (HI (upper)) (versus average summer minimum specific humidity; HI (lower)) on the main results of the study.